Journal of Imaging Science and Technology® 51(1): 1–22, 2007.

Improved Pen Alignment for Bidirectional Printing

Edgar Bernal and Jan P. Allebach
School of Electrical and Computer Engineering, Purdue University, West Lafayette, IN 47907-1285
E-mail: eabernal@purdue.edu

Zygmunt Pizlo
Department of Psychological Sciences, Purdue University, West Lafayette, IN 47907-1285

Abstract. *The quality of the prints produced by an ink jet printer is highly dependent on the characteristics of the dots produced by the ink jet pens. While some literature discusses metrics for the objective evaluation of print quality, few of the efforts have combined automated quality tests with subjective assessment. The authors develop an algorithm for analyzing printed dots and study the effect of the dot characteristics on perceived print alignment. The authors establish the perceptual preferences of human observers via a set of psychophysical experiments.*

[DOI: 10.2352/J.ImagingSci.Technol.(2007)51:1(1)]

INTRODUCTION

The advent of low cost, photo-quality ink jet printers has raised the need for an objective means of determining print quality that is consistent with what the end-user perceives. High level quality metrics have been specified in the International Association for Standardization/International Electrotechnical Commission (ISO/IEC) guidelines on hardcopy print assessment.[1] These guidelines include metrics for four distinct categories of printed areas: line and character metrics, solid fill metrics, tint solid metrics, and background field metrics. Other metrics that enable the quantification of performance aspects relevant to ink jet printers have also been proposed. These aspects include color registration, color consistency, modulation transfer function (MTF), text quality, sharpness,[2] dot quality, and line quality.[3,4]

Multiple efforts have been made to automate the process of image quality assessment both during product development[5] and manufacturing,[6] and for benchmarking and competitive analysis.[4,7] The ultimate objective of these initiatives is to provide the ability to measure a large volume of prints and, at the same time, achieve the repeatability and objectivity that visual inspection-based processes lack.

Attempts have also been made to characterize and reduce print quality defects inherent to ink jet technology, such as the inability to achieve uniformity in areas of solid color because of banding,[8] printing artifacts derived from incorrect dot placement,[9] dot shapes and sizes that differ from the ideal,[10] and the presence of tails and satellites due to aerodynamic effects.[11]

Low level models have also been used to improve the quality of printed halftone images. There are two approaches to the development of such model-based algorithms.[12] The first approach uses models that reflect the actual process whereby the digital halftone is transformed to colorant on the page. For example, models for the laser beam, exposure of the organic photoconductor, and the resulting absorptance on the paper have been embedded into the Direct Binary Search (DBS) halftoning algorithm for electrophotographic (EP) printers,[13] showing good improvement over regular binary DBS with tone correction. The second approach is largely based on characterization of the halftone image as it exists on the printed page. For example, analytical and stochastic models for EP printer dot interactions have been incorporated in the DBS halftoning algorithm,[14] yielding enhanced detail rendition and improved tonal gradation in shadow areas. For ink jet printers, the displacement and profile of individual dots were measured and the conditional pixel statistics were calculated.[15] These results were then applied to the DBS halftoning algorithm to develop an ink jet printer model that reduced the visual artifacts caused by systematic and random errors in dot placement.

An ink jet printer places marks on the page by means of a print head that contains columns of nozzles through which ink is fired. The nozzles are fired in a carefully controlled manner as the print head moves back and forth across the page. Careful alignment of the dot patterns printed in successive passes across the page is critical to perceived print quality. The aim of this paper is to study the effects of the printed dot characteristics on the perception of ink jet pen alignment via an approach that relies both on automated image analysis tools and psychophysical experiments. We develop a set of image analysis tools to characterize many attributes of printed dots, including alignment. We also examine the relationship between physical alignment and perceived alignment. This paper focuses on the HP DeskJet 6540 (Hewlett-Packard Company, 3000 Hanover St., Palo Alto, CA 94304-1185) high resolution ink jet printer with plain paper, but the methodology is generally applicable to other ink jet printers and paper types as well.

The structure of the paper is as follows: we first give an overview of the ink jet printing process. We then describe the calibration of the image capture device and the design of

Received Jul. 31, 2006; accepted for publication Oct. 11, 2006.
1062-3701/2007/51(1)/1/22/$20.00.

the tools that enable alignment measurement and dot analysis. We present some experimental results obtained from the application of the dot analysis tool to test prints. We proceed to describe the set of psychophysical experiments that were performed on alignment perception. Finally, we give our conclusions.

PRELIMINARIES

Figure 1 illustrates the operation of a typical ink jet printer. The paper is advanced through the unit by a series of rollers driven by a stepper motor. A carriage transports the pen or printhead back and forth across the page. The printhead consists of one or more columns of nozzles through which drops of ink are fired onto the surface of the paper. Printed dots reveal artifacts that depend on print options such as print resolution, speed, directionality, and the number of printing passes over each pixel on the paper. A *print mode* specifies the set of such print options with which a document is printed. The pixels that are printed in a given pass across the page comprise a subset of the pixels in a horizontal band with height equal to the height of the print head. This horizontal band of pixels is called a *swath*. In the single-pass print modes, the printhead passes only once over each position on the paper, so the swaths do not overlap. For a multipass print mode with N passes, the paper only advances a fraction $1/N$ of the height of the printhead between passes. With the single pass print modes, misalignment between adjoining swaths is especially visible. With multipass modes, the misalignment is masked to some extent by the overlapping swaths. Typically, a print mode with one pass, a higher printhead velocity, and lower resolution is used for draft quality printing and a mode with multiple passes, a lower printhead velocity, and a higher resolution is used for the highest quality printing. To achieve print resolutions that are lower than the native resolution of the print mechanism, two or more dots are printed in a cluster for each pixel.

In this paper, we are primarily interested in draft quality printing of black and white documents using a single pass mode. This *modus operandi* implies that there is a tradeoff between print speed and print resolution. To see this, consider the simpler case in which the printhead has only one column of nozzles and is moving at a speed of v inches per second (ips) across the page. Suppose also that the maximum frequency at which the nozzles can be fired is f firings/sec. Then, the closest distance at which two horizontally adjacent dots can be printed is $d=v/f$ in., and the maximum resolution that can be achieved with that particular print mode is $1/d$ dots per inch (dpi). Since f is fixed for a given printhead, the print resolution is inversely proportional to the print speed. In unidirectional print modes, the pen only fires ink while it is traveling in one direction across the page (either while traveling from left to right or from right to left), while in bidirectional print modes, successive swaths are printed in opposite directions.

When printing at a resolution of 300 dpi, the DeskJet 6540, which has a pen with vertical nozzle-to-nozzle spacing of 1/600 in., renders a single dot as two vertically adjacent dots. However, given the high nozzle firing frequency required to print at high carriage speeds, some of the nozzles fail to fire ink occasionally, which results in some single dots being printed on the page. Figure 2 shows typical single and double dots printed at a carriage speed of 30 ips and scanned at 7000 dpi with a QEA IAS-1000 Automated Image Analysis System (Quality Engineering Associates Inc, 25 Adams Street, Burlington, MA 01803).

Figure 3 shows the appearance of a typical dot printed with a single-pass, 300 dpi resolution print mode with different carriage speeds and printing directions. It illustrates the fact that as print speed increases, the dot shape becomes more asymmetric, and thus more dependent on the printing direction. Other artifacts that are related to print speed are

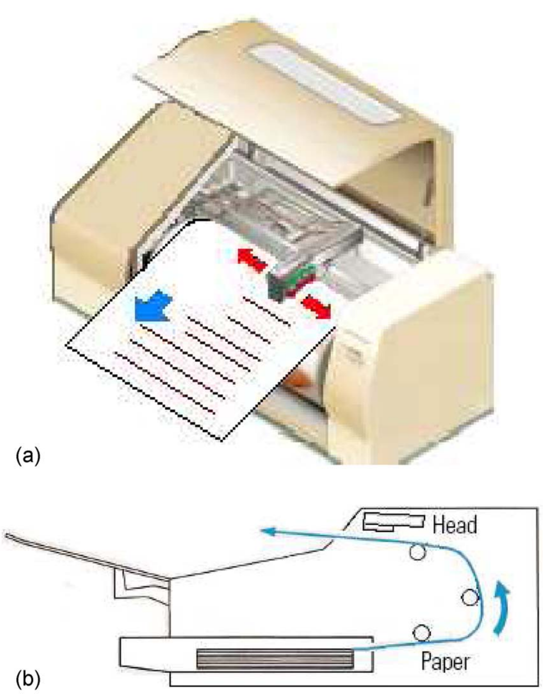

Figure 1. Operation of an ink jet printer: (a) the 3-D view illustrates the movement of the printhead and (b) the cross-section illustrates the paper path.

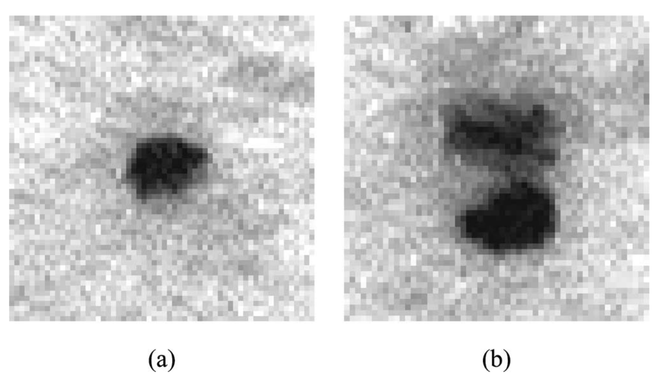

Figure 2. Effect of print resolution on dot appearance: (a) single dot and (b) double dot printed with 300 dots per inch (dpi), 30 inches per second (ips), right-to-left print mode. Scanned at 7000 dpi with QEA IAS-1000.

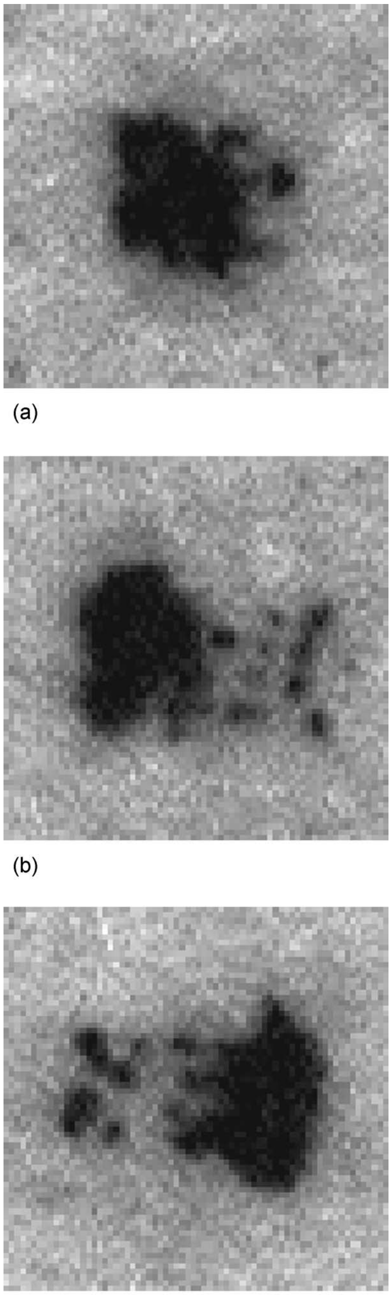

(a) (b) (c)

Figure 3. Typical dot printed at 300 dpi: (a) 15 ips left-to-right print mode, (b) 45 ips left-to-right print mode, and (c) 45 ips right-to-left print mode. Scanned at 7000 dpi with QEA IAS-1000.

tails and satellites, which occur when the drop of ink breaks up as it exits the print nozzle. If the secondary droplet breaks away completely from the main droplet, it forms a satellite [see Fig. 4(a)], and if it breaks away only partially, it forms a tail [see Fig. 4(b)]. Tails and satellites usually trail the main dot relative to the direction of travel of the pen. Since there is a tradeoff between print quality and print speed and also because the media characteristics and page content impact the choice of print mode that will yield the best print quality, a number of different print modes are typically designed for an ink jet printer. The specific effect of the print modes on the dot attributes will be described in detail later.

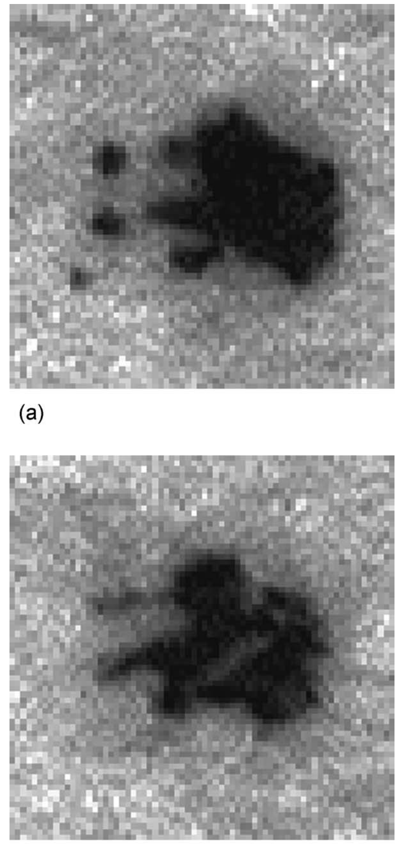

(a) (b)

Figure 4. Other artifacts due to high print speeds: (a) satellites and (b) tails on dots printed at 300 dpi, 60 ips, right-to-left print mode. Scanned at 7000 dpi with QEA IAS-1000.

The process of printing a vertical line with a single-pass, bidirectional mode is illustrated in Fig. 5 for a simplified printer architecture. The printhead contains nozzles (in this case, 3 columns of 8 nozzles each) that fire the colorant onto the page. Typically, a real printhead would contain many more nozzles. For example, the black ink printhead for the HP DeskJet 6540 printer contains 4 columns of 168 nozzles each. The two-dimensional image of the line (including the blank regions surrounding the line) is encoded onto a *print mask*,[16] which consists of a two-dimensional array of 0's and 1's. A 1 indicates firing the nozzle at that particular position and a 0 indicates no firing. In the case illustrated by Fig. 5, the upper segment of the vertical line is printed on the left-to-right pass of the pen and the lower segment is printed on the right-to-left pass. The size of each swath is determined by the distance between the top and bottom nozzles in the pen.

Vertical alignment within a swath is readily achieved via the fixed spatial positions of the nozzles in the printhead, and between swaths by the correct advancement of the paper. Horizontal alignment within a swath is also readily achieved by virtue of the fixed spatial configuration of the nozzles in the print head, and through synchronized firing of

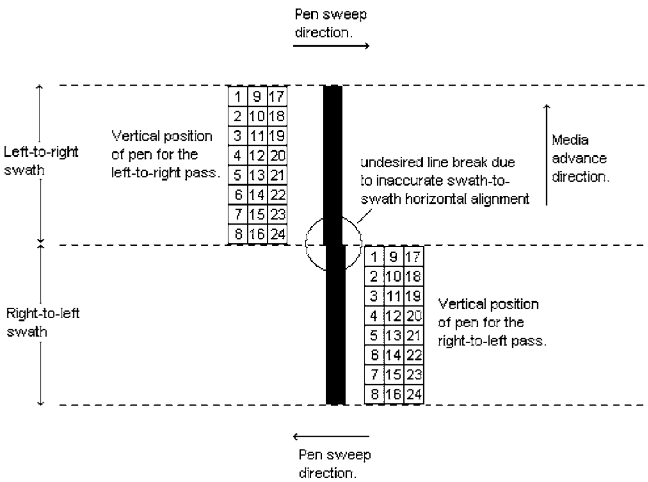

Figure 5. Illustration of the process of printing a vertical line in a single-pass, bidirectional print mode, with a 24-nozzle pen. The vertical position of the pen with respect to the media changes from swath to swath as the paper is advanced.

the nozzles while the print head moves at constant velocity. Between swaths, horizontal alignment depends on the timing of the start of the firing of nozzles at the initial edge of the page. Consequently, swath-to-swath horizontal alignment is the factor that ultimately determines whether or not the print appears aligned to the viewer. Figure 5 illustrates the situation where an undesired line break is produced due to inaccurate horizontal alignment between swaths. In reality, however, the line segments printed on each of the swaths are more complex than those depicted in the figure. This is because of the dot irregularities and the fact that the relationship between the main dot and tails or satellites is reversed from raster to raster. Thus, the task of achieving accurate swath-to-swath alignment requires knowledge of how the human viewer actually perceives the position of the main dot/satellite or main dot/tail pair.

The ability of the human viewer to detect misalignment has been widely studied in cases where the line segments are displayed or printed with ideal devices. The just noticeable angular offset between two line segments is called *Vernier acuity*.[17] It has been found that the discriminable offset ranges from 5 to 10 seconds of arc (2.9×10^{-4} in. to 5.8×10^{-4} in. at a viewing distance of 12 in.), which is much less than the distance of 25 seconds of arc between foveal receptors. However, few studies have considered the case where the lines are composed of irregular dots. Patel et al. found that thresholds for asymmetric irregular shapes were higher than those for regular dots.[18] Since dots become more irregular as the print speed increases, evaluation of alignment perception at high print speeds (45 ips and above) is of particular interest. Also, since higher print speeds imply lower print resolutions, the test resolution was fixed at 300 dpi for the fastest print modes. This is the highest resolution achievable at the highest print speed for this printer.

To enable automatic measurement of the print characteristics, we designed a test pattern that is printed with an ink jet printer and scanned with the Aztek Premier high resolution drum scanner (Aztek Digital Imaging, 13765-F Alton Parkway, Irvine, CA 92618). We developed a software tool that classifies and quantifies the printed dot characteristics and calculates the relative position of adjacent swaths from the scanned version of the test pattern. To match the perceived attributes and the measured quantities, we used a set of test pages encoded in a low level printing language as the stimuli in the psychophysical experiments. The low level printing language allows fine tuning of the swath-to-swath offsets as well as print speeds and print directions.

PREPROCESSING

The alignment measurement procedure consists of printing, scanning, and processing a test pattern in order to get dot placement information. Even though the images obtained with the QEA System are sharper than those obtained with the Aztek Scanner, the latter was chosen for this task due to its larger field of view at high resolutions. The alignment analysis tool relies on averaging dot positions across a large number of dots that cover a printed area of approximately 1 in.$\times$1 in. The Aztek Scanner is capable of capturing a region of 8.5 in.$\times$11 in. regardless of the scanning resolution, while the field of view of the QEA is less than 0.1 in. $\times$0.1 in. at 8000 dpi. In this section, the scanner calibration procedure that allows the mapping of the scanner grayscale output into absorptance is described. Also, the design of the test pattern and the initial processing to find boundaries between dots are presented.

Scanner Calibration

Scanner calibration is the process whereby device-dependent scanner RGB values are converted into values of a device-independent color space such as CIE XYZ.[19] The scanner calibration was performed as suggested in Ref. 20:

1. A TIFF file containing 17 half-inch square test patches with gray values ranging from 0 to 1 was generated.
2. The TIFF file was printed using the printer driver's halftoning technique at 600 dpi. The same printer and the same colorant (K) used in the alignment study were used in the calibration process.
3. The luminance values of the patches were measured with a calibrated Gretag SPM-50 (Gretag Data and Image Systems, Althardstrasse 70, CH-8105 Regensdorf, Zürich, Switzerland) spectrophotometer. Five measurements were taken for each patch and the results were averaged. The resulting luminance was converted to absorptance (0–1) values and then rescaled to fall in the range 0–255.
4. The patches were scanned at 1000 dpi with the Aztek Premier drum scanner. The resulting patch images were cropped to avoid edge effects, and the average grayscale value of each patch was found.
5. The scanner data S was fitted to the spectrophotometer data G using an exponential function of the form $G=a_1(S/255)^{\gamma}+a_2$ by minimizing the mean-

squared error between the function output and the data points. The resulting coefficients were $a_1 = 262.48$, $\gamma = 1.23$, and $a_2 = 5.02$.

6. Before any scanned image is processed, it is calibrated using this mapping. The raw data and the fitted curve are shown in Fig. 6.

Test Pattern Design and Dot Boundary Calculation

The first step toward pen characterization consists of designing a test pattern with attributes that enable the measurement of the quantities of interest. In our case, we are interested in being able to measure swath-to-swath alignment and to quantify dot characteristics such as shape, size, elongation, and presence or absence of artifacts, such as tails and satellites.

The test pattern we designed is a 600×600 pixel grid where only every 20th row and 20th column contains a printed dot. Hence, there are a total of 900 dots in the printed test pattern. In order to facilitate scanner focusing and to stabilize the pen's nozzle firing, a 50-pixel-wide solid frame surrounds the central grid, and a 400 pixel $\times 400$ pixel solid black region is placed on each side of the frame. Figure 7 shows the designed test pattern.

The test pattern is printed in the desired print mode (the dot analysis tool works for any print mode, as long as the test pattern complies with the specifications listed above) and then scanned at a resolution of 8000 dpi with the Aztek Premier Scanner. The scanned image is processed to produce a binary segmentation mask image that indicates the presence or absence of ink at every pixel. The threshold for the image binarization is calculated according to Otsu's method,[21] an unsupervised approach that minimizes the intra-class variance of the black and white pixels. Figure 8 shows a portion of the scanned test pattern and its corresponding segmentation mask.

With the aid of the segmentation mask, boundaries between rows and columns are found, and boundaries delimiting dot regions are determined. Boundaries between columns are determined by vertically projecting the data of the binary image and finding the points of the projection that are greater than zero, as illustrated in Fig. 9(a). The process is similar for row boundaries, except that the projection is done horizontally. The boundaries for a dot's cell are determined by intersecting the boundaries of the row and the column to which the dot belongs, as illustrated in Fig. 9(b). The centroid of each dot is then calculated based on the spatial distribution of ink absorptance throughout the dot's corresponding cell. If the cell of the dot is defined by the coordinates (x_1, y_1) and (x_M, y_N), as shown in Fig. 9(b), then its horizontal center of mass is given by

$$C_x = \frac{\sum_{n=1}^{N} \sum_{m=1}^{M} I(m,n) x_m}{\sum_{n=1}^{N} \sum_{m=1}^{M} I(m,n)}, \tag{1}$$

where $I(m,n)$ is the absorptance value of the image at the pixel with coordinates (x_m, y_n). Similarly, the vertical center of mass is given by

$$C_y = \frac{\sum_{n=1}^{N} \sum_{m=1}^{M} I(m,n) y_n}{\sum_{n=1}^{N} \sum_{m=1}^{M} I(m,n)}. \tag{2}$$

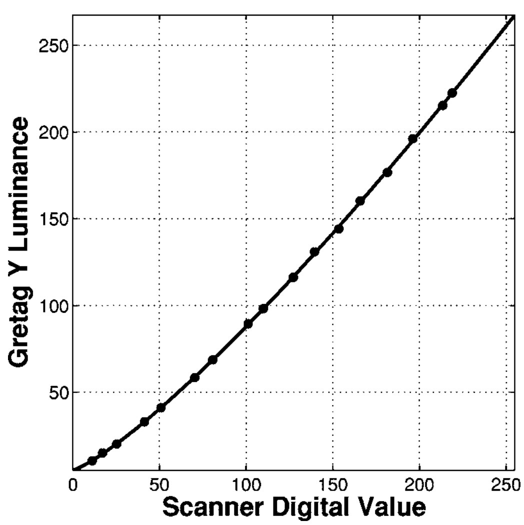

Figure 6. Raw data and fitted curve for the Aztek Premier Scanner.

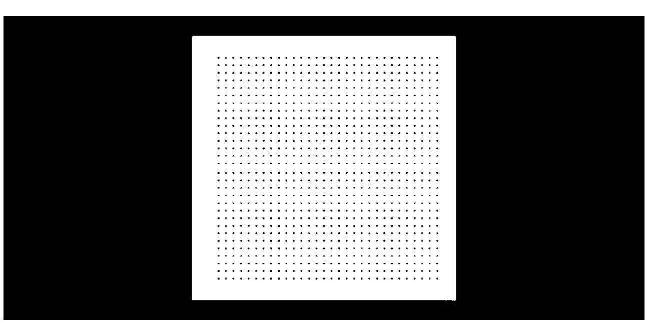

Figure 7. Test pattern for printhead and alignment characterization.

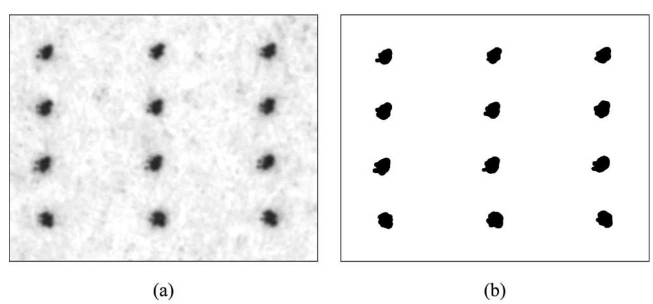

Figure 8. Cropped version of (a) test pattern printed with 15 ips, bidirectional print mode and scanned at 8000 dpi with Aztek Premier Scanner and (b) corresponding binary mask.

DOT ANALYSIS

In this section, the procedure for misalignment measurement, dot analysis, and pen characterization is presented. First, we will describe the procedure for measuring misalignment from scanned images of the test target. Then, we will discuss the algorithms that classify dots into double and single dots, segment double dots, and detect tails and satellites and separate them from the main dots. These algorithms were applied to images obtained with the Aztek Scanner.

Misalignment Measurement

Since the height of each swath is known, it is possible to determine the regions in the image that correspond to different swaths by segmenting the image file into horizontal stripes with height equal to the height of one swath. Then, if the upper and lower halves of the test pattern shown in Fig. 7 are positioned in adjacent stripes, misalignment can be estimated by calculating the offset between the average horizontal position of the dots in the upper half of the pattern and the average horizontal position of the dots in the lower half of the pattern. If $C_{x_{i,j}}$ is the horizontal center of mass of the dot in the ith row and jth column, then the average swath-to-swath misalignment is given by

$$\overline{\Delta C_x} = \frac{1}{450}\sum_{j=1}^{30}\left\{\sum_{i=1}^{15}\left(C_{x_{i,j}} - C_{x_{i+15,j}}\right)\right\} \tag{3}$$

because rows 1 to 15 belong to the upper swath and rows 16 to 30 belong to the lower swath, and there are a total of 450 dots in each swath. This approach, however, yields estimates that are highly dependent on the image skew, which can occur during both printing and scanning.

In order to account for the effect of image skew, the angle of skew must be estimated. This is done by fitting a straight line to each of the rows of dot centroids via orthogonal regression[22] and averaging the slopes of the set of straight lines thus obtained. The new reference columns are found by fitting straight lines to each of the columns of dot centroids, with the constraint that they should be perpendicular to the line describing the skew of the image. The orthogonal distance of each of the centroids to its respective reference column is calculated. The average of these distances across dots on each swath is computed to find the average offset of each swath. The total misalignment is estimated by computing the difference between the average offset of the upper swath and the average offset of the lower swath. Figure 10 illustrates the process of skew estimation and misalignment measurement.

Dot Classification

As seen earlier, double dots are inherent to 300 dpi resolution print modes when printing with a 600 dpi resolution

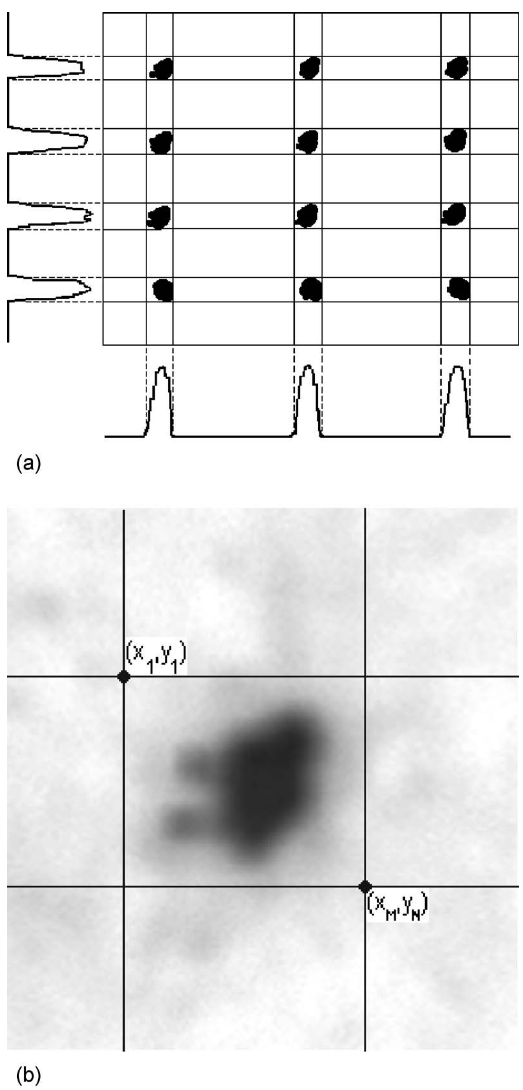

Figure 9. (a) Finding boundaries between rows and columns and (b) finding the centroid of a dot.

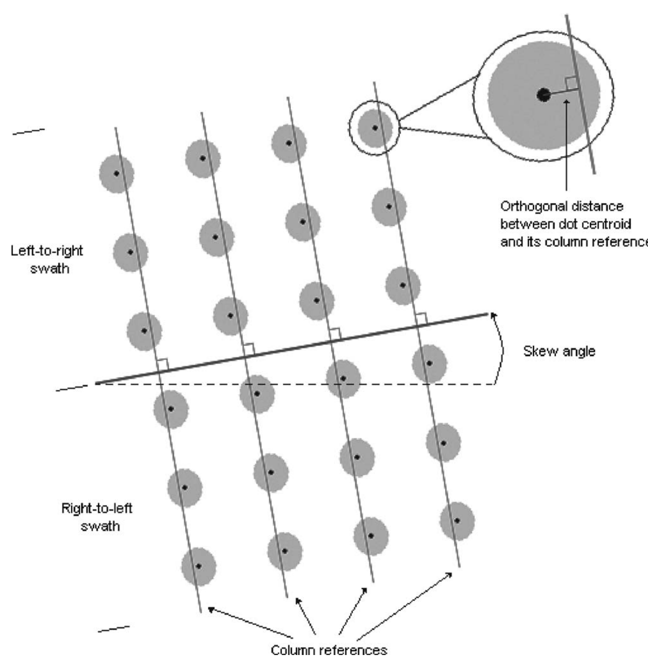

Figure 10. Skew estimation and misalignment measurement.

printhead. Also, as the print speed increases, tails and satellites appear more frequently. Identifcation of the main attributes of the printed dots plays a fundamental role in the dot analysis process. The process of dot classification into single and double dots consists of coding the most relevant information of the dot image and comparing it to a database of previously coded training samples to find the one that most resembles the dot. To this end, the principal components of the distribution of the information embedded in the set of training dot images must be found.[23]

The simplest approach consists of representing the $N\times N$ image of the dot as an $N^2\times 1$ vector in an N^2-dimensional space. Then, if the set of training samples consists of the images $I_1, I_2, \ldots, I_M$, we can represent each image I_i as a vector $\mathbf{\Gamma}_i$. The average image is given by

$$\mathbf{\Psi} = \frac{1}{M}\sum_{i=1}^{M} \mathbf{\Gamma}_i. \tag{4}$$

The principal components of the set of training images are the eigenvectors of the covariance matrix

$$\mathbf{C} = \frac{1}{M}\sum_{i=1}^{M} (\mathbf{\Gamma}_i - \mathbf{\Psi})(\mathbf{\Gamma}_i - \mathbf{\Psi})^{\mathsf{T}}. \tag{5}$$

This set of vectors is the basis of the new feature space.

Let $\{\mathbf{v}_1, \mathbf{v}_2, \ldots, \mathbf{v}_K\}$ denote the set of K eigenvectors corresponding to the K largest eigenvalues of $\mathbf{C}$. This set will be the basis of the new eigenspace and any $N\times N$ arbitrary dot $\mathbf{\Gamma}$ can be approximated by a linear combination of its elements as $\mathbf{\Gamma}\approx\sum_{i=1}^{K}\alpha_i\mathbf{v}_i+\mathbf{\Psi}$, where $\alpha_i=\mathbf{v}_i^{\mathsf{T}}(\mathbf{\Gamma}-\mathbf{\Psi})$. Since the basis of the space is fixed, an image $\mathbf{\Gamma}-\mathbf{\Psi}$ can be represented by the vector of its coefficients, $\mathbf{\Omega}=[\alpha_1\cdots\alpha_K]$. The training of the algorithm consists of calculating the coefficients $\mathbf{\Omega}_1, \mathbf{\Omega}_2, \ldots, \mathbf{\Omega}_M$ that correspond to the images $\mathbf{\Gamma}_1, \mathbf{\Gamma}_2, \ldots, \mathbf{\Gamma}_M$ whose class is known. To classify a new dot $\mathbf{\Gamma}$, its corresponding coefficients $\mathbf{\Omega}$ are found and the Euclidean distance $\epsilon_i=\|\mathbf{\Omega}-\mathbf{\Omega}_i\|$ is calculated for $i=1,\ldots,M$. The new dot is assigned to the same class as dot j, where

$$j = \arg\{\min_i\{\epsilon_i, i = 1,2,\ldots,M\}\}, \tag{6}$$

i.e., we find the dot j from the training set that is closest to the new dot in terms of the K coefficients and assign the new dot to the same class to which dot j belongs.[24] In our case, the training set consisted of five single dots and five double dots, and the classification stage worked with four coefficients, which implies that $M=10$ and $K=4$. Figure 11(a) shows a sample image that illustrates the results of the dot classification stage. Dots surrounded by a single frame were identified as single dots and dots surrounded by a double frame were identified as double dots. The performance of the classification stage was found to be 100% accurate among the group of patterns tested. This group was comprised of at least 100 test patterns, each composed of 900 dots. Figure 11(b) shows a scatter diagram of the coefficients α_1 and α_2 for the single and double dot training samples and for the single and double dots in Fig. 11(a). It can be seen that in this two-dimensional feature space, the projection coefficients form two clusters, one corresponding to each dot class. This is why a simple metric such as the Euclidean distance yields a good classification performance.

Dot Bisection

All dots identified as double dots have to go through the process of bisection. This is necessary because in the end we want to know the characteristics of individual dots. Given the large number of dots present in a single test pattern, there is a need to implement an efficient segmentation algorithm. Caselles et al.[25] and Kass et al.[26] devised segmentation algorithms based on active contours that lock onto image

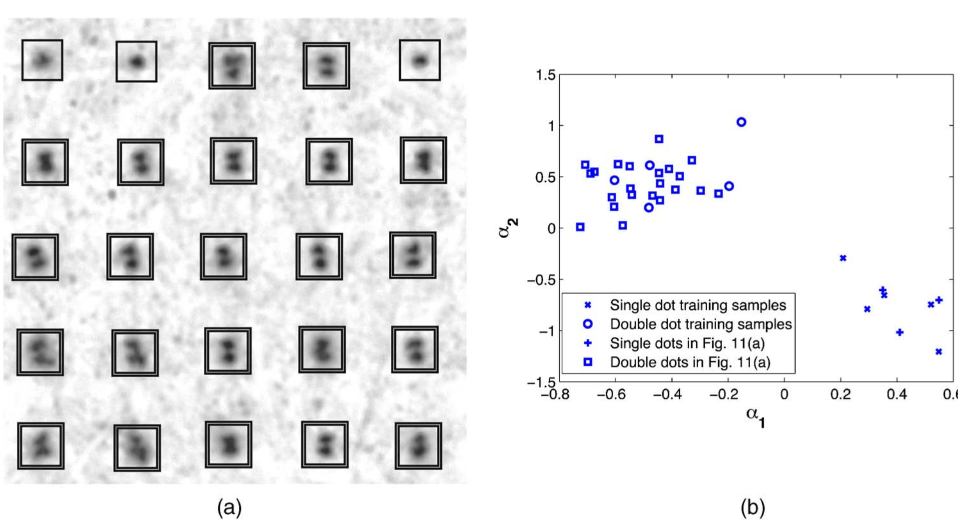

(a) (b)

Figure 11. Operation of the dot classification stage: (a) Cropped region of a test image after the dot classification stage. Dots surrounded by a single frame were identified as single dots and dots surrounded by a double frame were identified as double dots. (b) Scatter diagram of coefficients α_1 and α_2 for the training samples and for the dots in Fig. 11(a).

features such as lines and edges. *A priori* knowledge of the topology of the desired final solution imposes an important constraint on the possible approaches and allows for the design of a faster algorithm than those belonging to the active contour class, which were designed for a general class of images.

Our solution is a fixed-topology, multi-resolution approach to the "snakes" active contour model proposed by Kass et al.[26] This model modifies the shape of the solution until a contour with minimum total energy is found. Let the contour be described parametrically as $v(s)=[x(s),y(s)]$, $s \in [0,1]$. Let $\{s_i\}_{i=1}^{N}$ be a set of real numbers such that $0 \leqslant s_1 < \cdots < s_N \leqslant 1$. Then the total energy of the contour can be approximated by

$$E = \sum_i \alpha E_{\mathrm{cont}}(s_i) + \beta E_{\mathrm{curv}}(s_i) + \gamma E_{\mathrm{image}}(s_i), \qquad (7)$$

where E_{cont} is the energy due to the continuity of the contour components, α is its corresponding scaling factor, E_{curv} is the energy due to curvature or bending of the contour, β is its corresponding scaling factor, E_{image} is the energy due to the image gradient on the contour components, and γ is its corresponding scaling factor. Minimizing the continuity energy corresponds to finding a contour in which the distance between elements is small. Minimizing the curvature energy is equivalent to finding a contour with the smallest curvature possible. Lastly, minimizing the image energy corresponds to finding a contour with elements located in small gradient image regions. Minimizing the overall energy corresponds to finding a compromise between the three energy values regulated by the three scaling constants.

As will be seen later, neither the continuity term (which regularizes the interpixel distances) nor the curvature term (which controls the smoothness of the contour) imposed in the snakes approach were utilized herein, since they are implicit in the implementation of our algorithm. For the external energy term, image absorptance rather than image gradient, as suggested by Kass et al.,[26] was chosen. This is

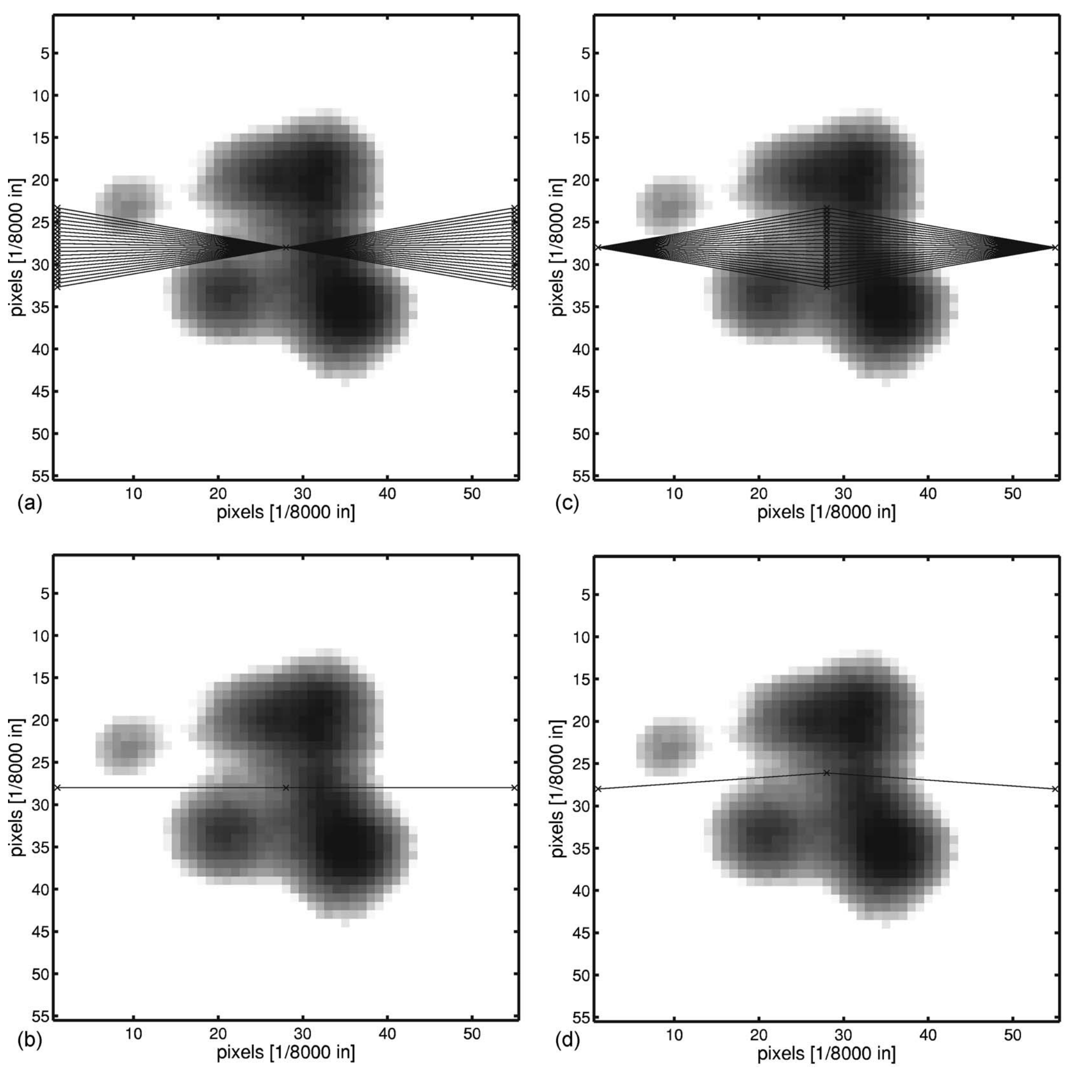

Figure 12. First stage of bisection process: (a) candidates for endpoints of the bisecting contour, (b) selected endpoints, (c) candidates for third component of the contour, and (d) selected point.

because the bisecting contour should lie in the lightest path between the two dark regions that correspond to each of the dots.

Figure 12 illustrates the evolution of the dot bisection process. In the first stage of the process, the line segment with the lowest integrated absorptance per unit length between the left boundary of the dot image and the dot centroid is found. The leftmost vertex of the bisecting contour is the one at which this particular segment originates. The line segment with the lowest integrated absorptance per unit length between the dot centroid and the right boundary of the dot image is also found. The rightmost vertex of the bisecting contour is the one at which this particular segment terminates. This step is illustrated in Fig. 12(a), which shows the set of candidates for contour endpoints and their respective line segments. Figure 12(b) shows the selected vertices. The third vertex of the contour is the point equidistant to the endpoints such that the line segments between it and the endpoints have the least integrated absorptance per unit length. Figure 12(c) shows some of the points in the set of candidates for a new vertex of the contour and the corresponding line segments. The average absorptance per unit length between each candidate point and both of the endpoints of the contour is calculated. The point that defines the segments with the least integrated absorptance per unit length is kept, as shown in Fig. 12(d). Note that the candidate points for new vertices are all located on the line segment that lies halfway between the endpoints and which is perpendicular to the line connecting the two endpoints. Thus, they are all equidistant to both endpoints. Also, note that the search is limited to a specific angle, called the angle of sweep. In the case illustrated in Fig. 12, the angle of sweep was set to ±15°.

In the subsequent stages of the algorithm, the same procedure is implemented between intermediate contour vertices. The multiresolution effect is a natural consequence of the fact that as the procedure advances, the energy of the active contour is minimized on smaller regions of the image. The distance between the contour vertices is determined by the number of stages in the procedure: the higher the num-

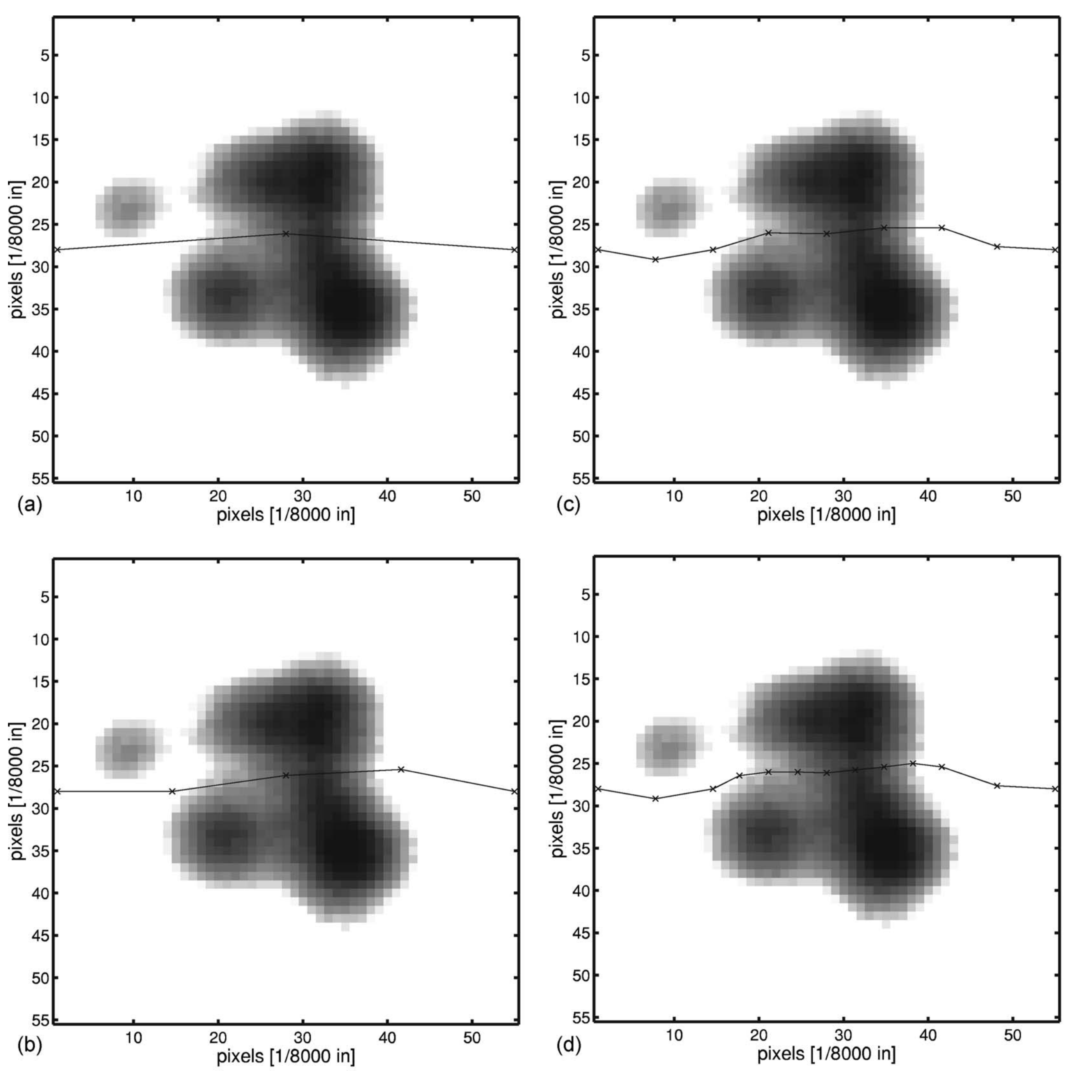

Figure 13. Evolution of bisection process after stages (a) 1, (b) 2, (c) 3, and (d) 4.

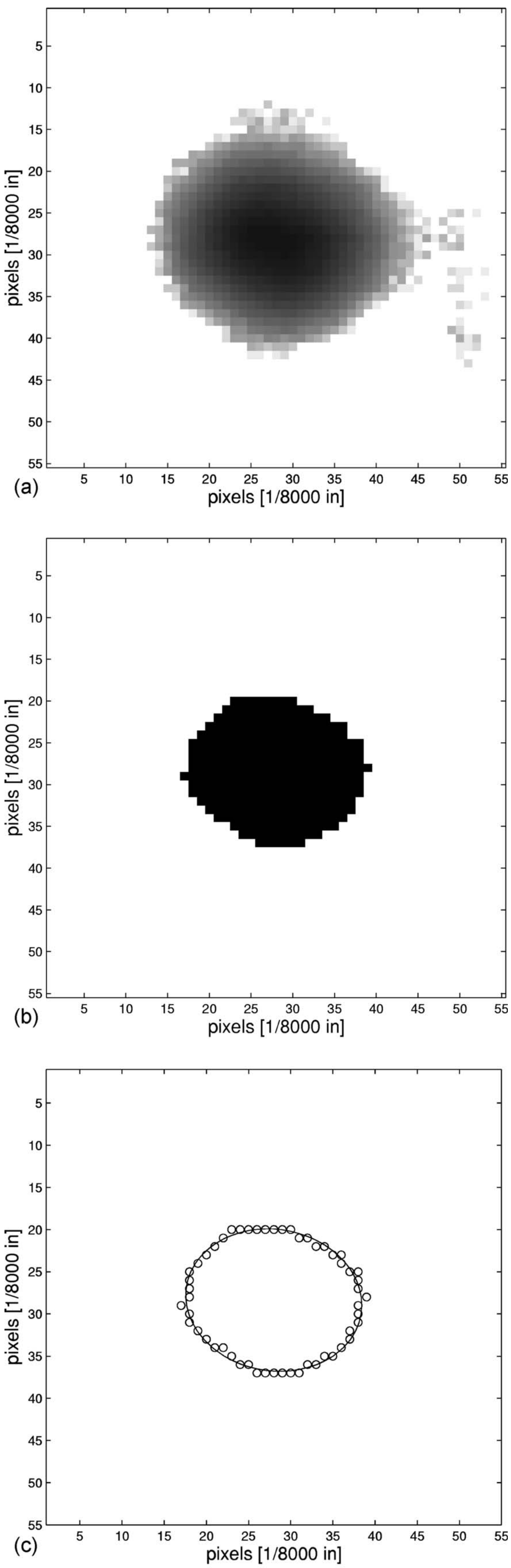

Figure 14. Illustration of ellipse fitting (a) grayscale image of dot, (b) binary dot, and (c) dot outline and fitted ellipse.

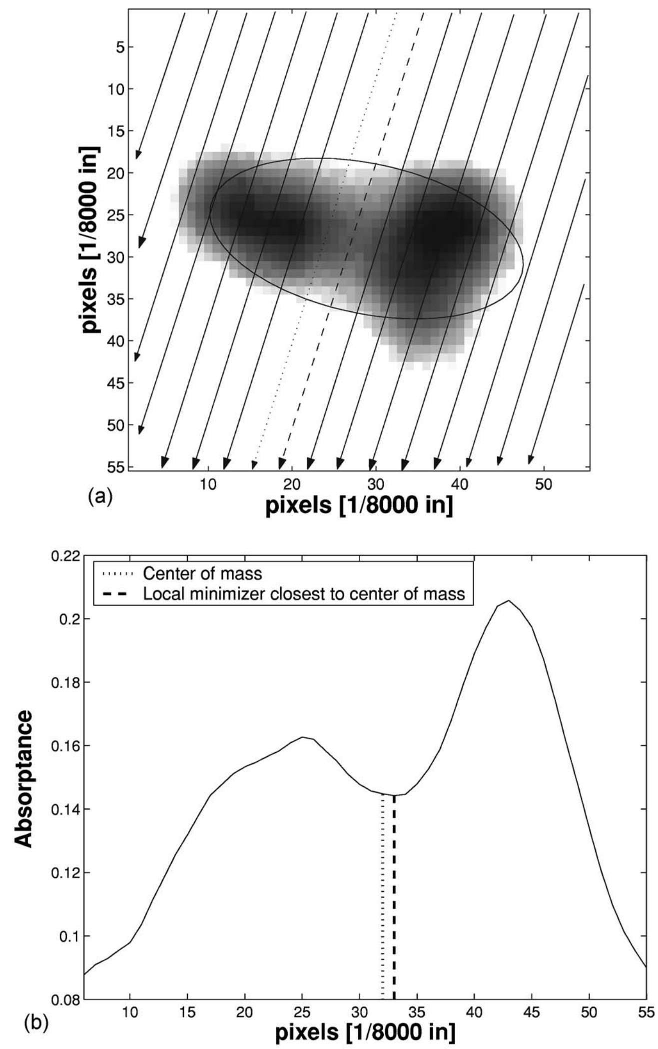

Figure 15. Initialization of tail detection algorithm: (a) fitted ellipse for single dot with a tail and direction of projections orthogonal to major axis of ellipse and (b) projected absorptance profile and positions of center of mass and local minimum in profile.

ber of stages, the higher the number of vertices in the contour, and thus the smaller the distance between vertices. The curvature characteristics of the contour are determined by the magnitude of the angle of sweep illustrated in Fig. 12(a). The larger the magnitude of that angle, the less smooth the contour can be. Thus, the continuity and curvature constraints are implicit in the implementation of the algorithm. Figures 13(a)–13(d) illustrate the evolution of the process.

Ellipse Fitting

Ellipse fitting is a basic task in pattern recognition because it describes the data in terms of a geometric primitive, thus reducing and simplifying its representation. In our case, ellipse fitting is used to estimate dot eccentricity, aspect ratio, and orientation. Historically, techniques for ellipse fitting are divided into two main approaches: clustering[27,28] and least-squares fitting.[29,30] While clustering methods are robust to outliers and can detect multiple primitives at once, they are computationally expensive and have low accuracy. On the

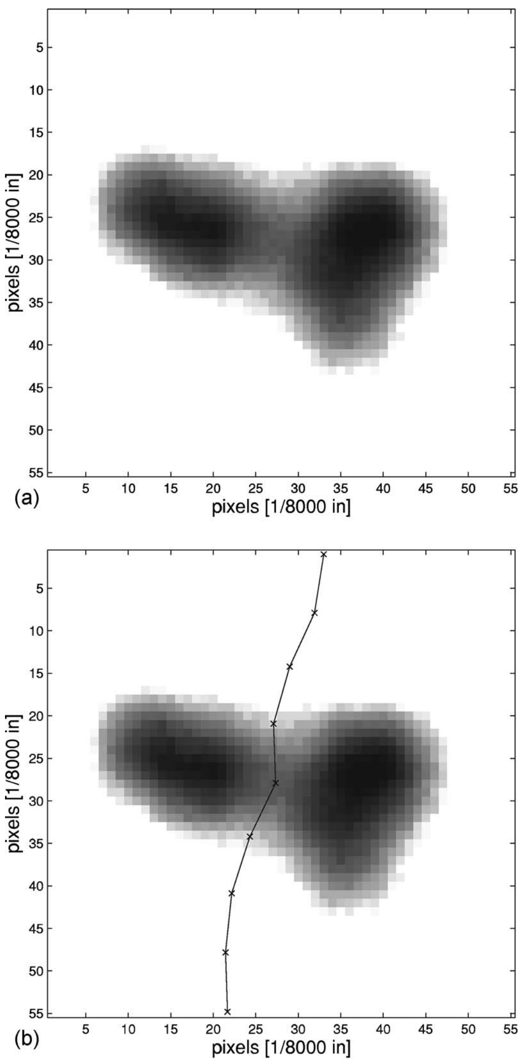

Figure 16. Tail detection algorithm: (a) single dot with a tail and (b) tail segment.

other hand, the least-squares methods are fast and accurate, but can only fit one geometric shape at a time and are more sensitive to outliers.[30] We found that the model proposed by Halif and Flusser,[30] which is an improved version of that proposed by Fitzgibbon et al.,[29] performed accurately and efficiently enough for our purposes. A short description of the method can be found in the Appendix (Appendix available as Supplemental Material on the IS&T website, www.imaging.org). The ellipse is fitted to the set of coordinates of the pixels that belong to the dot outline defined by the binary image of the dot, as shown in Fig. 14. The binary image of the dot is obtained by thresholding its grayscale image in the same manner as the binary segmentation mask is obtained from the grayscale scanned image (as described in section entitled "Test Pattern Design and Boundary Calculation"). From the ellipse coefficients, quantities such as dot aspect ratio and orientation are estimated.

Tail Detection

Tail and satellite dots manifest themselves in a way very similar to that in which double dots appear on the printed page:

Table I. Information provided for each single dot.

Output	Format
Location of dot's center of mass	2×1 vector of double precision floating point numbers
Total integrated absorptance of the dot	Double precision floating point number
Coefficients of the ellipse fitted to the dot outline	6×1 vector of double precision floating point numbers
Information of whether dot has a tail or not	Binary number
If dot has a tail, the location of the components of the tail-segmenting contour	2×9 array of double precision floating point numbers
If dot has a tail, the location of the main dot and tail's centers of mass	2×2 array of double precision floating point numbers
If dot has a tail, the total integrated absorptance of the main dot and of the tail	2×1 vector of double precision floating point numbers

there is a region of low absorptance between two regions of higher absorptance. In the case of double dots, these regions correspond to the two main dots, while in the tail/satellite problem, they correspond to the main dot and the tail or satellite. The main difference between the two is the fact that the direction of the segmenting contour that separates the tail or the satellite from the main dot is perpendicular to the orientation of the dot. From the ellipse-fitting stage, we can estimate the orientation of the main dot by the inclination of the main axis of the ellipse that best fits the points on the outline of the dot.

Figure 15(a) shows a dot with a tail and its fitted ellipse. An absorptance profile is obtained by projecting the dot absorptance in the direction perpendicular to the ellipse orientation, as indicated by the arrows. Figure 15(b) shows the profile obtained for this particular dot. For instance, the projected absorptance value corresponding to the path highlighted by the dashed gray (black) arrow in Fig. 15(a) is the point in the profile of Fig. 15(b) marked with the dashed gray (black) line. Starting at the point in the profile that corresponds to the dot's center of mass [see dashed gray line in Fig. 15(b)], a search for a local minumum is performed [see dashed black line in Fig. 15(b)]. The existence of a local minimum in the profile indicates the presence of a tail. If there is at least one local minimum, the position of the local minimum closest to the center of mass is found. In order to decrease the false alarm rate in the tail detection process, the decision that a tail is present is made only if the value of the profile at this local minimum is at least 20% smaller than the maximum value of the profile.

The tail-segmenting contour is initialized at the extreme points of the line segment whose projection yielded that particular local minimum [in this case, the segmenting contour is initialized at the end points of the dashed black arrow in Fig. 15(a)]. The subsequent stages of the tail separation process are the same as in the dot bisection process: at each stage, the point equidistant to the endpoints, such that the line segments between it and the endpoints have the least integrated absorptance per unit length, is found and added to the contour. This strategy makes the overall procedure for separating the main dot and its tail robust to errors in the initial estimation of the local minimum based on the projected absorptance. Figure 16 shows the results of the tail detection algorithm applied to a single dot with a tail.

EXPERIMENTAL RESULTS FOR DOT SHAPE ANALYSIS

In this section, some of the results gathered from the application of the dot analysis tool to different test pages are presented. The objective of the tests was to establish the variability of the dot characteristics from pen to pen for a sample population of pens, and from print mode to print mode for a single pen.

Output of Dot Analysis Tool

Pen alignment has an important impact on print quality, and the precision with which alignment is controlled impacts product engineering and cost. Dot shape characteristics impact both the appearance of the printed page and the way alignment is perceived. Therefore, in order to thoroughly study how alignment is perceived by human viewers, we must first understand how dot shape characteristics vary with the print mode for a single pen. However, these results will only be meaningful if we first establish that printing properties across a population of pens for a given print mode remain more or less stable. Thus, we first examine this aspect of the pen characteristics.

The dot analysis tool takes the scanned image of the test pattern (see Fig. 7) printed with the HP DeskJet 6540 and processes it in the manner described in the preceding section. The output of the analysis tool is a set of text files that contain all the information required to extract the characteristics of each dot in the printed pattern. For each dot, the information of whether it is single or double is provided. If the dot is double, the location of the 13 components of its bisecting contour is included in the form of a 2×13 vector of double precision floating point numbers. From this point on, double dots are treated as two individual single dots. Then, for each single dot, the information contained in Table I is provided. Another of the outputs of the dot analysis tool is an image that illustrates all the information enumerated above in a graphic manner superimposed on the original

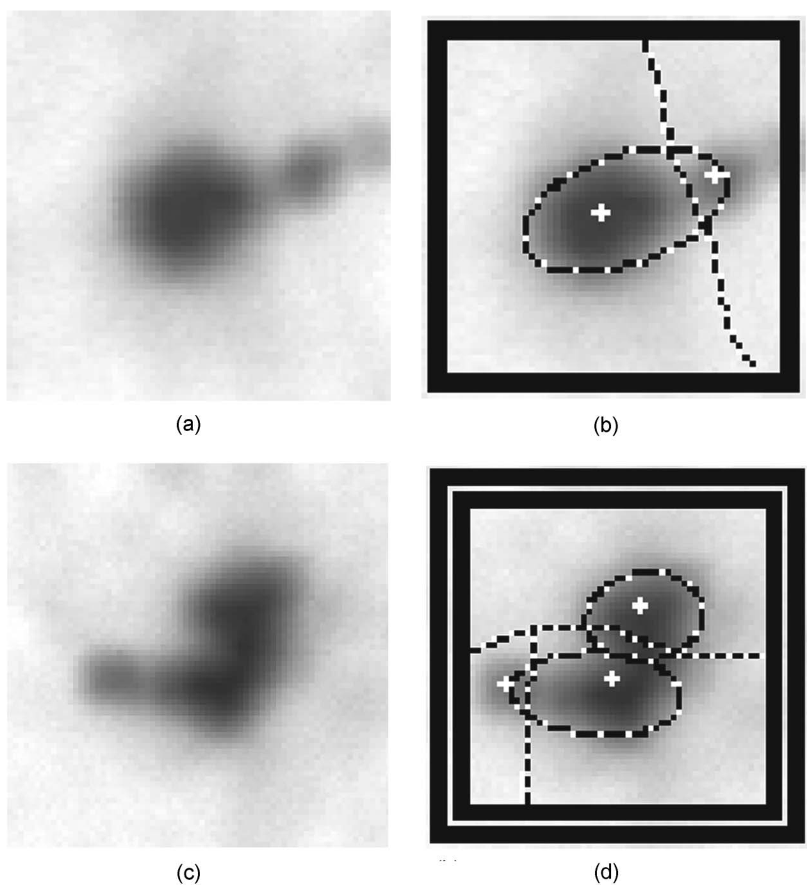

Figure 17. Illustration of the operation of the analysis tool: (a) original scanned single dot, (b) result of analysis of single dot, (c) original scanned double dot, and (d) result of analysis of double dot. The type of black frame surrounding the dot corresponds to the type of dot. The dotted lines are the bisecting and tail-segmenting contours. The dashed lines are the fitted ellipses. The white crosses are the main dot and tail/satellite centroids.

Table II. Parameters for the five different print modes.

Print mode No.	Directionality	Carriage speed
1	Unidirectional	15 ips
2	Bidirectional	15 ips
3	Bidirectional	30 ips
4	Bidirectional	45 ips
5	Bidirectional	60 ips

image. Figure 17 shows sample input and output images for both single and double dots. The output images show the ellipse fitted to the dot, the tail-segmenting contour, and the centers of mass of the main dot and of the tail.

In order to allow for controlled variation of the dot characteristics, the test targets had to be encoded into Printer Control Language (PCL) commands. PCL commands embed printing attributes such as print resolution, carriage speed, and print directionality into the print job before sending it to the printer. The process of encoding a page in the PCL language consists of breaking the image file into horizontal stripes with height equal to the height of a swath. Then, each image file is converted to a PCL file that specifies the carriage speed, directionality of the print, resolution, and the number of nozzles to use. The PCL files corresponding to each of the image swaths are then sent sequentially to the printer by means of a proprietary software tool that allows the horizontal offset between swaths to be changed in steps as small as 1/13 of 1/600 in.

Two printing attributes were varied throughout to obtain different dot characteristics: print speed and print directionality. A total of five different print modes were created. The parameters of each of the print modes are listed in Table II. A specific class of dots corresponds to each of these print modes. In order to identify the main differences between the type of dot produced by each print mode, the test target was printed and subsequently analyzed with the dot analysis tool.

Effect of Print Speed on Dot Characteristics

The first source of variability tested was the variability from pen to pen. Using the dot analysis tool, we were able to establish that the attributes of the printed dot remain more or less constant for a given print speed throughout a fairly large population of pens. We tested a population of 30 different pens and measured the characteristics of the printed dots for the 60 ips, bidirectional print mode. Figure 18 shows the resulting fraction of dots with a tail (measured as number of tails divided by number of dots) and dot aspect ratio (measured as the ratio of the ellipse's major to minor axes) for the pen population. Upon inspection of the plots, it becomes clear that there is not a significant variation of the dot characteristics from pen to pen, for a particular print mode.

Figure 19 shows the average dot profile for the right-to-left swaths at different print speeds. It becomes evident from the inspection of these images that as carriage speed increases, the average dot elongation increases and satellites and tails tend to grow. Figure 20 shows the effect of speed on the average dot aspect ratio and the fraction of dots with a tail and corroborates quantitatively the qualitative assertions concluded from the inspection of Fig. 19: as print speed increases, the average dot aspect ratio increases and the fraction of dots with a tail increases.

PSYCHOPHYSICAL EXPERIMENTS ON ALIGNMENT PERCEPTION

Psychophysical experiments allow us to draw conclusions about perception. The objective of this section is to make inferences about the effect of dot characteristics on perceived alignment from responses of human subjects in constant stimuli and signal detection experiments. The five print modes described in the section "Output of Dot Analysis

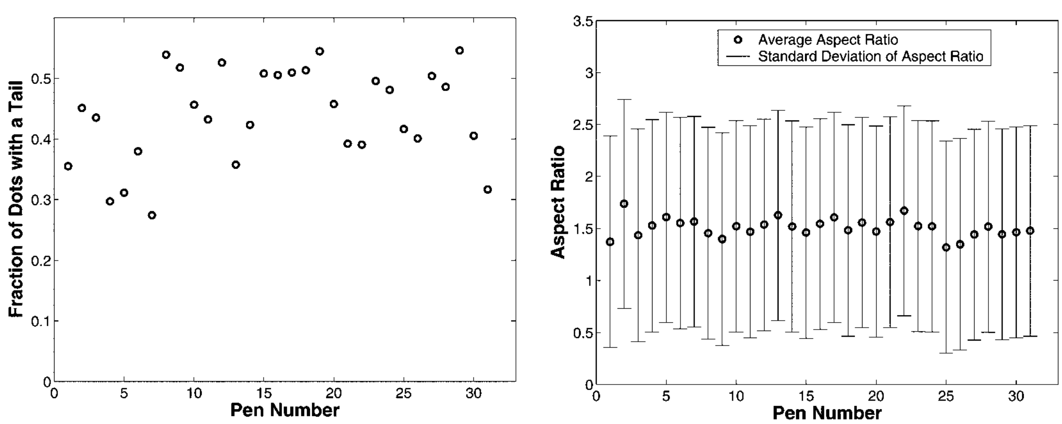

(a) (b)

Figure 18. Statistics for sample pen population averaged across all dots in the test pattern for each pen: (a) fraction of dots with a tail and (b) average dot aspect ratio.

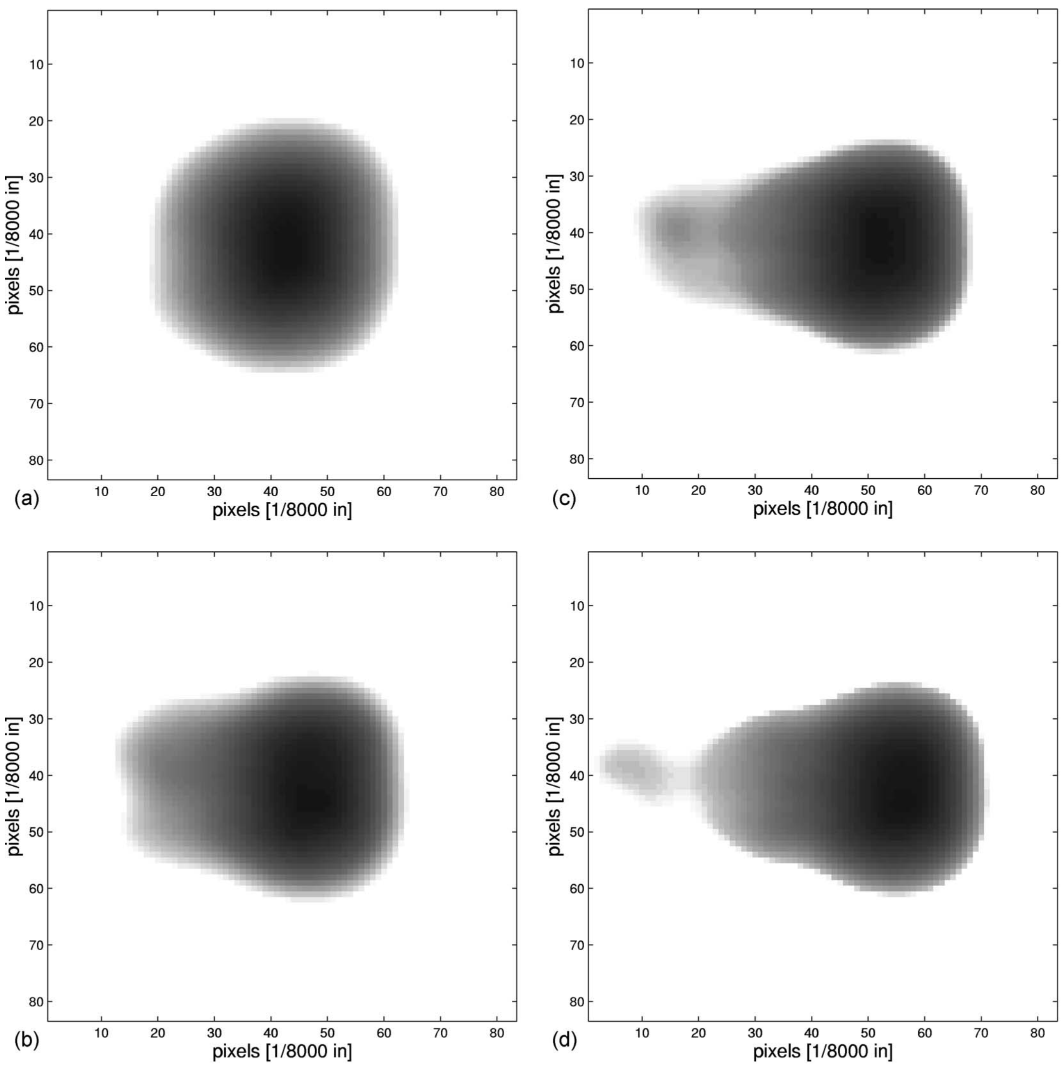

Figure 19. Average dot profiles for different print speeds: (a) 15 ips, (b) 30 ips, (c) 45 ips, and (d) 60 ips. As carriage speed increases, average dot elongation increases, and the likelihood of tails and satellites increases.

Tool" were used to print the test images shown to the subjects. The following sections describe the design and the results of the experiments.

Constant Stimuli Test

Recall from the section "Misalignment Measurement" that misalignment is measured as the average offset of the horizontal centroids in each column of dots in the upper swath with respect to the horizontal centroids in each column of dots in the lower swath, while taking into account the effects of skew (see Fig. 10). In this experiment, printed misalignment values ranging from 0/600 in. to 1.6/600 in. are chosen. Preliminary tests showed that this range was informative enough for our purposes since it contains values that are consistently perceived as aligned, consistently perceived as misaligned, and values that do not offer a clear choice. Thus, offset values that produce measured misalignment ranging from 0/600 in. to 1.6/600 in. were chosen to be tested. The actual measured misalignment values tested vary from print mode to print mode, since the only parameter we can change is the relative offset between swaths. A test image is printed for each of the offset values and shown to the subject. For this experiment, two test pages consisting of line-based drawings were used as test images (see Fig. 21). In order to measure printed misalignment for each test image, five test patterns arranged horizontally across the whole width of the page (see Fig. 22) were placed directly below each of the images and printed on the same page. The test patterns were hidden prior to the execution of the experiment. Image misalignment was estimated by averaging the misalignment across the five patches, and only images with alignment whose standard deviation across the five test patches was smaller than 0.1/600 in. were kept. The order of presentation was randomized and the subject was asked to answer whether he/she was able to detect misalignment in each of the test pages. A total of 16 subjects with normal or corrected to normal vision, who were students and/or staff

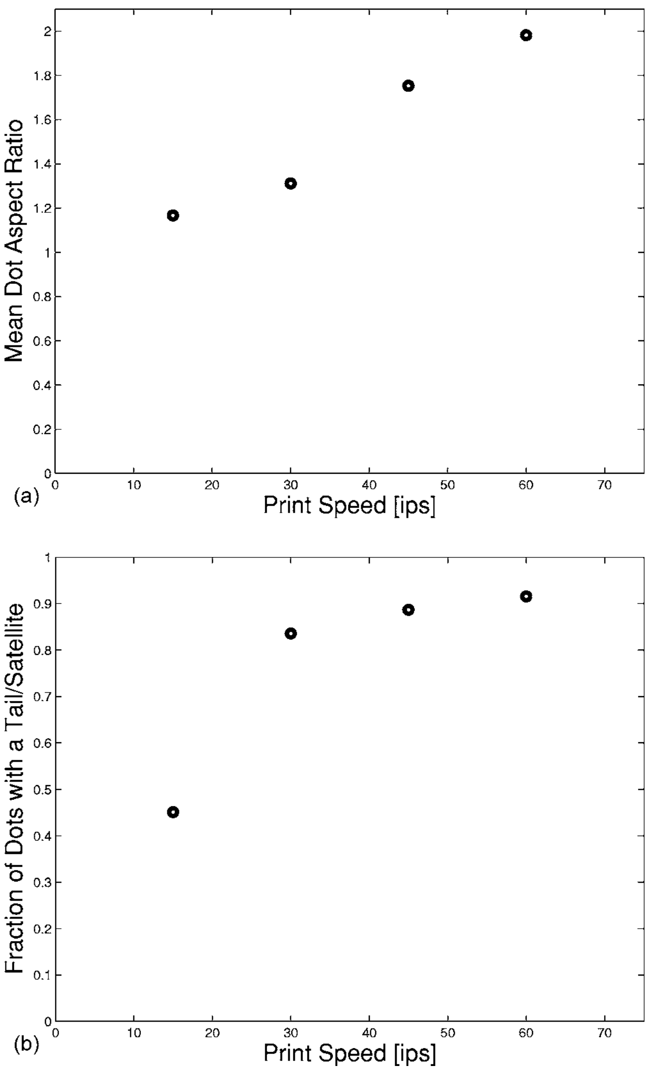

Figure 20. Effect of print speed on (a) average dot aspect ratio and (b) fraction of dots with a tail. As print speed increases, the average dot aspect ratio increases and the fraction of dots with a tail increases.

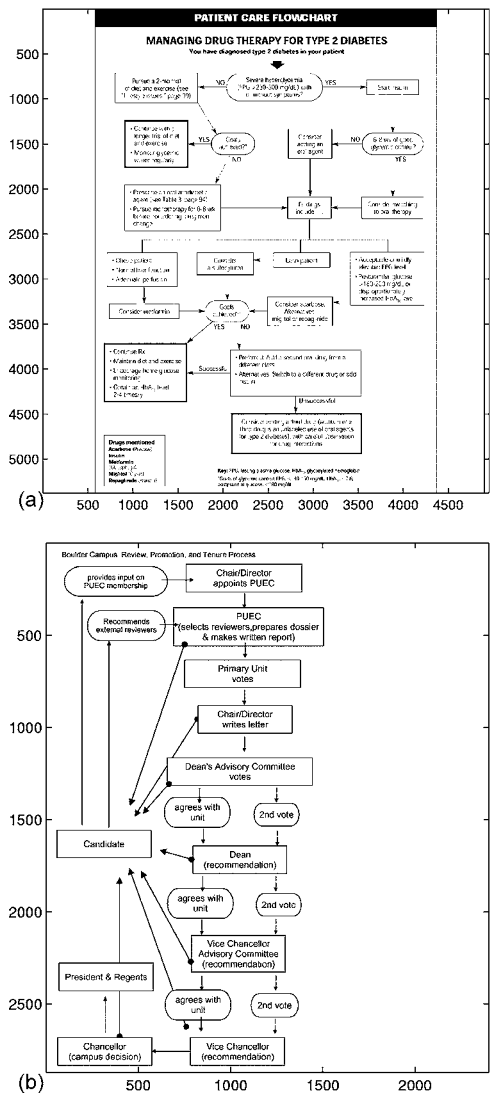

Figure 21. Test images used in constant stimuli test: (a) 600 dpi resolution image and (b) 300 dpi resolution image.

members at Purdue University, participated in this experiment.

The first test image was the 600 dpi resolution flowchart depicted in Fig. 21(a). Eleven versions of this image were printed with the 15 ips, unidirectional print mode, each version at a different misalignment value, for a total of 11 images. The second test image was the 300 dpi resolution flowchart depicted in Fig. 21(b). Eleven versions of this image were printed with each of the four remaining print modes, each version at a different misalignment value, for a total of 44 images. Therefore, the total number of stimuli for the experiment was 55. Each subject was free to change the viewing distance to the page and to take as much time as needed to give a response. However, it was found that the subjects tended to hold the pages at a viewing distance of 10 to 12 in., and that the average time to complete the experiment was less than 30 min.

The proportion of “Detected” responses across subjects for each misalignment amount was recorded and plotted against the corresponding misalignment value. The data

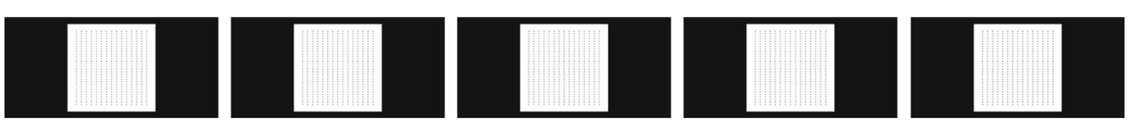

Figure 22. Arrangement of test patterns used to measure misalignment on test pages. These test patterns were printed below the images shown in Fig. 21 and were hidden during the psychophysical experiments. Figure 7 shows the detailed structure within each of the test patterns.

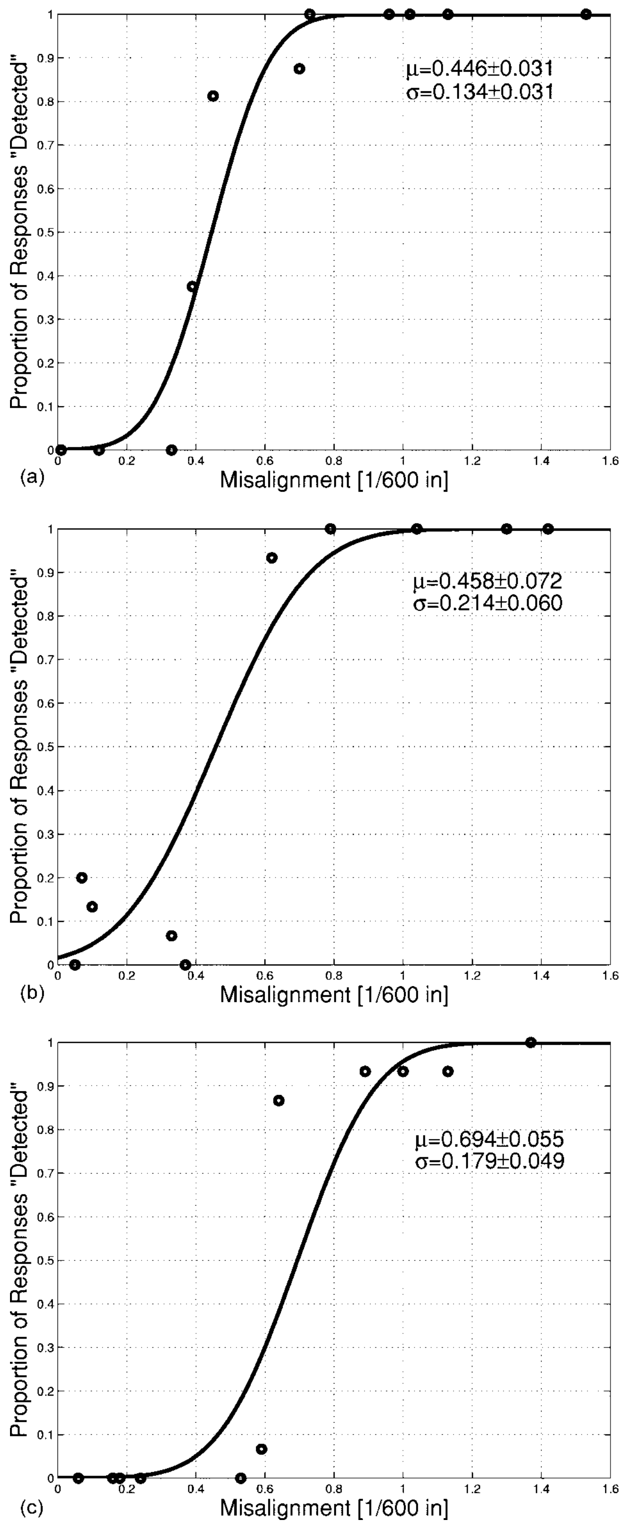

Figure 23. Average proportion of "Detected" responses across 16 subjects and corresponding psychometric curves for (a) 15 ips unidirectional, (b) 15 ips bidirectional, and (c) 30 ips bidirectional print modes. Both estimated parameters μ and σ and the corresponding standard estimation errors are included.

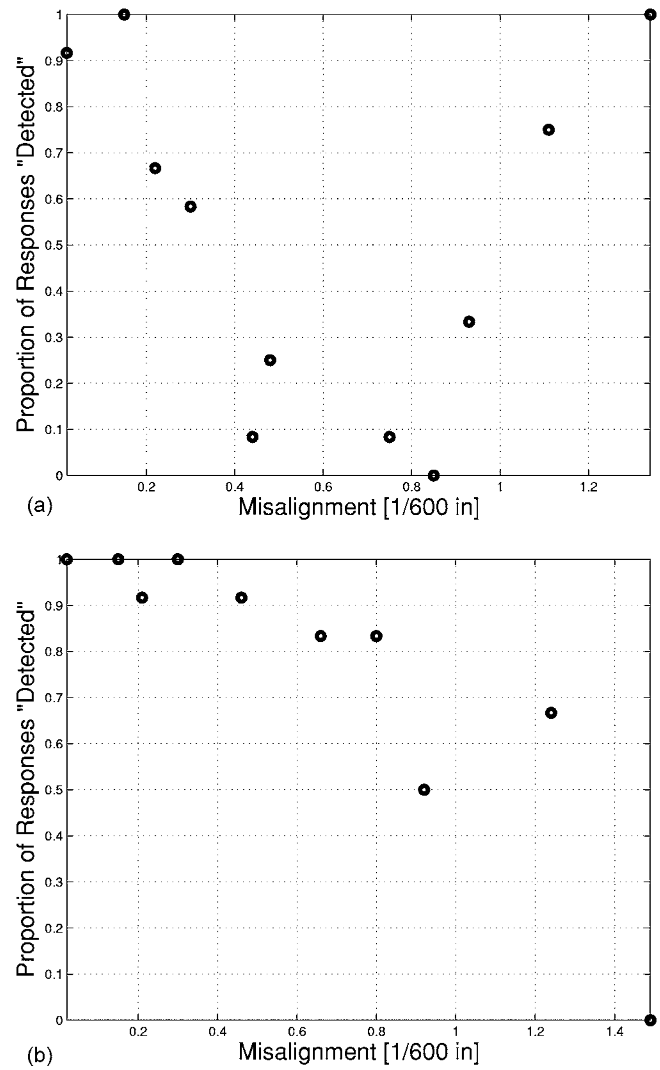

Figure 24. Average proportion of "Detected" responses across 16 subjects for (a) 45 ips bidirectional and (b) 60 ips bidirectional print modes. Standard probit analysis cannot be applied since the data points are not monotonic.

points were fitted with a cumulative Gaussian distribution by estimating the mean μ and standard deviation σ via Probit Analysis.[31,32] In this case, σ is related to sensitivity to changes in alignment: the larger its value, the less sensitive the subjects are. The parameter μ reflects both sensitivity to changes in alignment and response bias. Specifically, higher sensitivity leads to smaller values of μ. At the same time, however, the value of μ may depend on the subject's response criterion. For example, if the subject is conservative, that is, if he/she decides to the answer "Not Detected" when in doubt, μ will be larger.

Figure 23 shows the resulting curves and data points from the experiments corresponding to three print modes: 15 ips unidirectional, 15 ips bidirectional, and 30 ips bidirectional. Note that, as expected, the proportion of "Detected" responses increases as the misalignment value increases. This suggests that the point of perceived perfect alignment (the point at which the proportion of "Detected" responses is close to zero) coincides with the point of measured perfect alignment (the point at which measured misalignment is 0 in.). The plots include the estimated values for μ and σ as well as the standard error for each of the

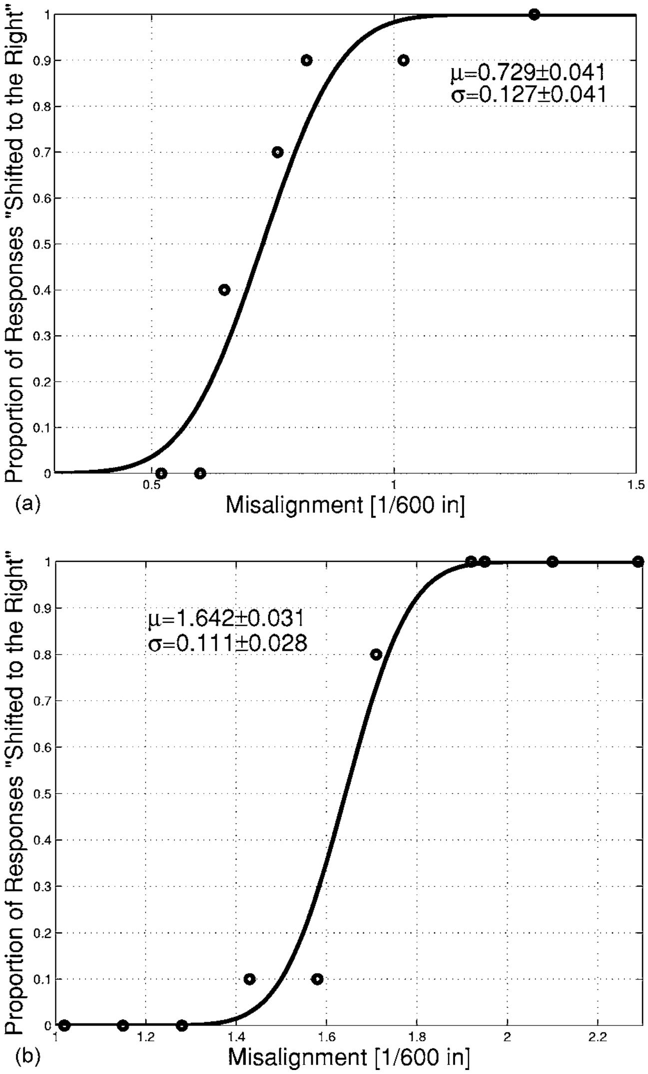

Figure 25. Average proportion of "Shifted to the Right" responses across ten subjects and corresponding psychometric responses for symmetric test with (a) 45 ips bidirectional and (b) 60 ips bidirectional print modes. Both estimated parameters μ and σ and the corresponding standard estimation errors are included.

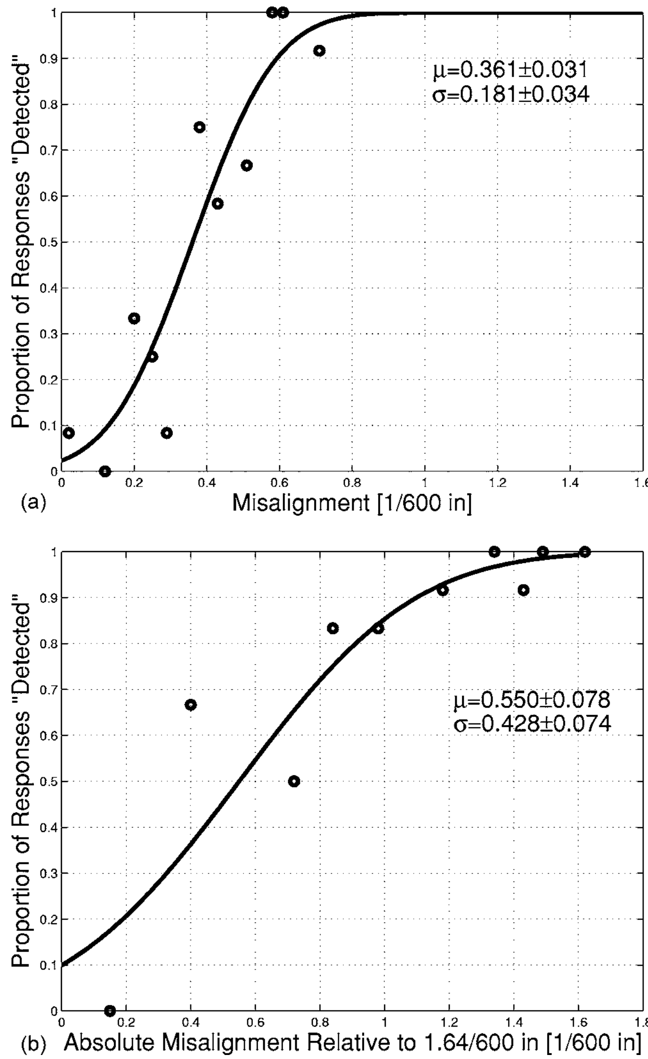

Figure 26. New psychometric curves for (a) 45 ips bidirectional and (b) 60 ips bidirectional print modes. Both estimated parameters μ and σ and the corresponding standard estimation errors are included.

parameters. Note that σ cannot be estimated reliably because there are almost no data points for which the proportion of detections is near 0.5. Most of the data points correspond to a proportion of "Detected" responses equal to 0 or 1. Therefore, only μ can be used as a measure of sensitivity, although it may confound sensitivity with response bias. From the graphs, we can conclude that the higher print speed leads to lower sensitivity.

Figure 24 shows the resulting data points from the experiments corresponding to the two remaining print modes: 45 ips bidirectional and 60 ips bidirectional. Note that the proportion of "Detected" responses was close to zero for measured misalignment that was not 0 in.: between 0.4/600 and 0.9/600 in. for the 45 ips print mode, and at 1.5/600 in. for the 60 ips print mode. This suggests that the point of perceived perfect alignment does not correspond to the point of measured perfect alignment. This is related to the fact that at higher print speeds, the dots are highly elongated and the dot's centroid does not correspond to the perceived center of the dot. Since the data points do not exhibit the monotonicity characteristic of a Gaussian curve, Probit Analysis cannot be applied directly.

In order to estimate the point at which alignment is perceived as perfect, a new set of constant stimuli tests was designed. For this experiment, vertical lines composed of two line segments with measured offsets near the points at which the psychometric curves reach their minimum value (0.75/600 in. for 45 ips and 1.50/600 in. for 60 ips) were printed. Seven values were chosen for the 45 ips print mode and ten values were chosen for the 60 ips print mode. A test pattern like the one in Fig. 7 was placed directly below the vertical line and printed on the same page to enable misalignment measurement. The test pattern was hidden prior to the execution of the experiment. The order of the presentations was randomized and the subject was asked to answer whether the lower segment was shifted to the left or to the

Table III. Stimulus response matrix.

	Yes	No
Large misalignment	Hits	Misses
Small misalignment	False alarms	Correct rejections

Table IV. Signal detection test results.

	mean (d')	stddev (d')	mean (c)	stddev (c)
15 ips bidirectional	1.45	0.27	−0.04	0.14
30 ips bidirectional	2.23	0.55	−0.05	0.33
45 ips bidirectional	1.92	0.31	−0.06	0.19
60 ips bidirectional	1.57	0.25	0.00	0.25

Table V. Estimated DL from signal detection test results.

	ΔS (1/600 in.)	mean (DL) (1/600 in.)	stddev (DL) (1/600 in.)
15 ips bidirectional	0.24	0.17	0.04
30 ips bidirectional	0.32	0.14	0.05
45 ips bidirectional	0.26	0.13	0.02
60 ips bidirectional	0.48	0.30	0.05

right with respect to the upper segment. A total of ten subjects with normal or corrected to normal vision, who were students and/or staff members at Purdue University, participated in this experiment. Once again, the subjects were allowed to change the viewing distance to the page and to take as much time as needed to give a response. Subjects took on average less than 15 min to complete the test.

The proportion of "Shifted to the Right" responses across subjects for each misalignment amount was recorded and plotted against the corresponding misalignment value. The data points were fitted with a cumulative Gaussian distribution by estimating the mean μ and standard deviation σ via Probit Analysis. The mean value of the fitted Gaussian curves in this symmetric design is the point of subjective equality (PSE), that is, the point of measured alignment at which the line is subjectively perceived to be aligned over a large number of trials. The PSE provides a better estimator of the point of perfect perceived alignment than the misalignment value at which the propotion of "Detected" responses is minimum in the plots depicted on Fig. 24. Figure 25 shows the resulting psychometric curves, along with their respective estimated parameters. The plots include the estimated values for μ and σ as well as the standard error for each of the parameters. These results demonstrate that the point of perceived perfect alignment does not correspond to the point of measured perfect alignment for the two print modes under consideration, as expected from the previous experiment.

Now that we have a good estimator for the PSE, we can go back to the results in Fig. 24 and study them properly. The PSE might be thought of as the new origin for the data points of the constant stimuli tests for the 45 and 60 ips print modes depicted in Fig. 24: as we move away from the PSE (0.73/600 in. for the 45 ips print mode and 1.64/600 in. for the 60 ips print mode) in either direction, the proportion of "Detected" responses increases. Thus, relocating the origin of the plots in Fig. 25 to the position of the PSE and plotting the data points at their absolute distance from the PSE results in a monotonic sequence, which allows the application of Probit Analysis. This is consistent with the 15 ips and 30 ips cases, in which the PSE is near 0 in., and the data points exhibit a monotonic behavior as we move away from the origin. Figure 26 depicts the new psychometric curves for the original tests for 45 and 60 ips bidirectional, with the origin shifted to the position of the PSE and the data points located at their absolute distance from the PSE. Note that the value of σ is considerably higher for the 60 ips case than for any other case (see Fig. 23 and Fig. 26). This suggests that subjects might be less sensitive to changes in alignment at this particular print speed.

Signal Detection Test

The Gaussian parameter estimators from the constant stimuli test might be affected by noise for a variety of reasons, including response bias (the tendency of a subject to respond "Detected" or "Not detected" for reasons other than the percept of the stimulus itself) and lack of informative data points (those for which the proportion of "Detected" responses differs from 0 and 1). The latter is a consequence of the finite resolution of the printing device, which only allows us to change alignment in fixed-size steps. Signal detection tests are an alternative to measure a subject's sensitivity (the equivalent to σ in the constant stimuli tests) that is less affected by response bias.[33]

The signal detection experiment we performed falls in the class of Yes-No experiments for sensitivity measurement. In particular, we are interested in measuring the ability to distinguish between two misalignment values, rather than the ability to detect the presence of misalignment, as in the constant stimuli test. To this end, test pages consisting of vertical lines were encoded in the PCL language. A test pattern like the one in Fig. 7 was placed directly below the vertical line and printed on the same page to enable misalignment measurement. The test pattern was hidden prior to the execution of the experiment. Two groups of test pages, each consisting of 20 pages, were printed with each of the print modes. The test images in one of the groups had smaller misalignment values than those in the other group. The standard deviation of the misalignment values within each group was less than 10% of the difference between the average alignment values of the two groups. The order of the presentations was randomized and the subject was asked whether the page belonged to the large misalignment group or not, one page at a time. A total of seven subjects with normal or corrected to normal vision, who were students and/or staff members at Purdue University, participated in this experiment. Each of the subject's responses was tabulated into a stimulus response matrix (see Table III). The subjects were free to choose the most appropriate viewing distance to the test pages, and to take as long as they desired to evaluate each page. Subjects took on average less than 20 min to go through the 40 images.

Since there are a total of 20 images in each group, the number of hits plus the number of misses equals 20 as well as the number of false alarms plus the number of correct rejections. Therefore, it is only necessary to work with two of the four numbers in order to obtain all pertinent information about a subject's performance. The following is a short description of the data analysis procedure.[33]

The *hit rate* (H) is the proportion of large misalignment trials to which the subject responded "Yes," and the *false alarm rate* (F) is the proportion of small misalignment trials to which the subject responded "Yes." A common measure of sensitivity in signal detection theory is d'. It is defined in terms of the inverse of the normal distribution function, z, as

$$d' = z(H) - z(F). \tag{8}$$

The sensitivity measure d' is unaffected by response bias. This is because if the subject has the inclination to give a particular answer, both $z(H)$ and $z(F)$ move in the same direction, e.g., if the subject gives preference to the "Yes" response, both $z(H)$ and $z(F)$ increase, but their difference does not change. The subject's preference to a particular response, or the response bias c, is estimated as follows:

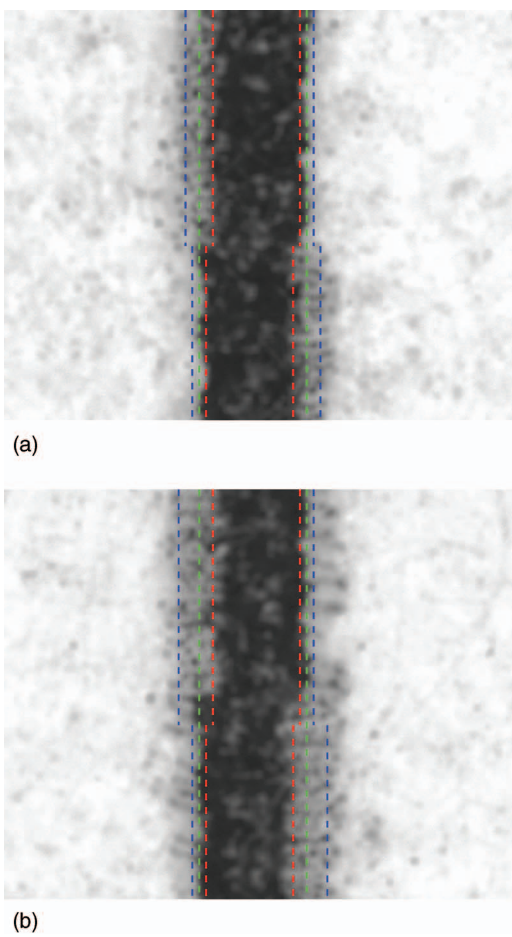

Figure 27. Interswath junctures of line segments consistently perceived as aligned for (a) 45 ips bidirectional (swaths displaced by 0.7/600 in.) and (b) 60 ips bidirectional (swaths displaced by 1.5/600 in.) print modes. The dashed lines correspond to the horizontal positions at which the vertically projected absorptance profiles in Fig. 28 take on the values 0.9 for the innermost (red) lines, 0.65 for the middle (green) lines, and 0.3 for the outermost (blue) lines. Scanned at 8000 dpi with QEA System.

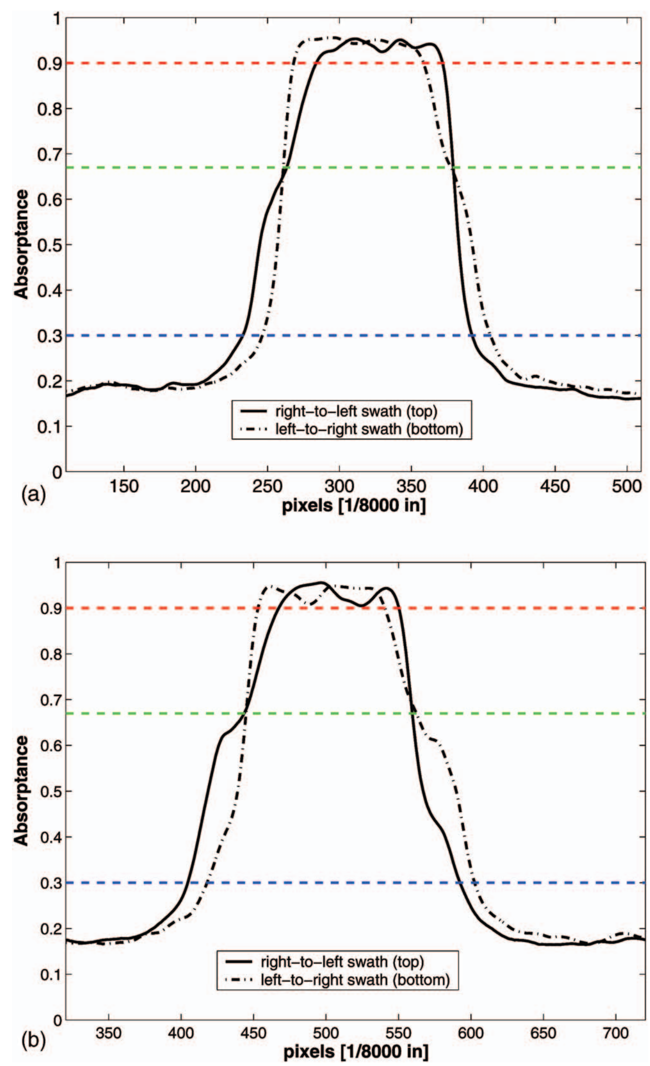

Figure 28. Absorptance profiles of interswath junctures that were consistently perceived as aligned for (a) 45 ips bidirectional and (b) 60 ips bidirectional print modes. Three selected absorptance levels are highlighted with dotted lines corresponding to the identical colored lines in Fig. 27. Note that both edges of the two interswath junctures intersect at the absorptance level 0.65 indicated by the green dotted line for both print modes.

$$c = -\frac{1}{2}[z(H) + z(F)]. \quad (9)$$

Table IV contains the d' and c results averaged across seven subjects. The values of c close to zero mean that there was little influence of bias on the recorded responses. Larger values of d' imply higher sensitivity to detect the *particular* difference in stimulus magnitude, here, the difference in alignment between the small misalignment and the large misalignment. Note that the differences in misalignment between the small and the large misalignment groups are different for each print mode. Therefore, in order to compare different print modes with respect to sensitivity, a parameter called difference threshold (DL) has to be calculated from d'.

The parameter DL is defined as the smallest difference in stimulus magnitude that can be reliably detected. If the Gaussian distribution is the correct model for the psychometric function, DL corresponds to the difference between stimuli magnitudes ΔS that produces $d'=1$. So, if d' is proportional to ΔS, DL is computed as follows:

$$\mathrm{DL} = \frac{\Delta S}{d'}. \quad (10)$$

The DL values estimated for each of the four print speeds are listed in Table V. It can be seen that the sensitivity of subjects to detect differences in alignment for the 15, 30, and 45 ips print modes is about the same, but the sensitivity for the 60 ips print mode is substantially lower (DL is larger).

Note that some knowledge of how subjects perceive alignment is required for proper design of the signal detection test. In particular, an appropriate value of ΔS is necessary for the test results to be meaningful. This is because if ΔS is too large, the subject may not produce any errors, and it would not be possible to estimate d'. On the other hand, if ΔS is too small, the subject would perform at a chance level and the estimator would yield $d'=0$. The information of how large ΔS should be chosen to be for each print mode is readily extracted from the constant stimuli test results. A good rule of thumb is to pick ΔS between σ and 2σ, where σ corresponds to the standard deviation of the psychometric curve from the constant stimuli tests.

Another important fact we had to keep in mind when designing the signal detection tests was that for the 45 and 60 ips, the PSE was not 0 in. In order for the signal detection test results to be meaningful, the misalignment values of both of the groups of prints must have the same sign relative to the PSE (they must both be located either to the right or to the left of the PSE). Otherwise, the resulting d' would be an underestimation of the subject's sensitivity. In fact, in the extreme case, the estimator would yield $d'=0$ even if the subject could reliably discriminate the two stimuli. For example, if misalignment values of 0.2/600 in. and 1.1/600 in. were chosen for the case shown in Fig. 24(a) (which corresponds to the constant stimuli test results for the 45 ips print mode), the subjects would judge the two levels as equally misaligned in a signal detection test, even though they are perceived as different: one is misaligned to the left and the other one is misaligned to the right.

Discussion

Point of Perceived Perfect Alignment

Some insight to the fact that the point of perceived alignment differs from that of measured perfect alignment can be gained by examining an actual interswath juncture that was consistently perceived as aligned by the subjects. As the alignment values change, the appearance of each separate swath remains unchanged, but the relative horizontal positions of adjacent swaths change. Therefore, subjects make their decision as to whether the print is aligned or not based on the appearance of the interswath junctures. This fact was corroborated by the subjects after each of the sessions. Figure 27 shows sample scanned interswath junctures from the images that were consistently perceived as aligned by the subjects for both 45 and 60 ips print modes. Recall that even though the horizontal center of mass of the segment from the upper swath is different from that of the segment from the lower swath, these particular arrangements were consistently perceived as aligned. To better understand the reasons why this happens, it is helpful to examine the average normal profiles of the upper and lower swath segments.

Figure 28 shows the vertically projected absorptance profiles for the line segments that belong to the right-to-left and left-to-right swaths in both of the junctures depicted in Fig. 27. In both cases, the profiles show the asymmetry that results from tails and satellites that trail the main dots on the side opposite the direction of movement of the pen. Note, however, that in spite of the asymmetry of the profiles, the points at which they intersect lie on a horizontal line at approximately the same magnitude of absorptance in both cases (see green dotted line in Fig. 28). This level of absorp-

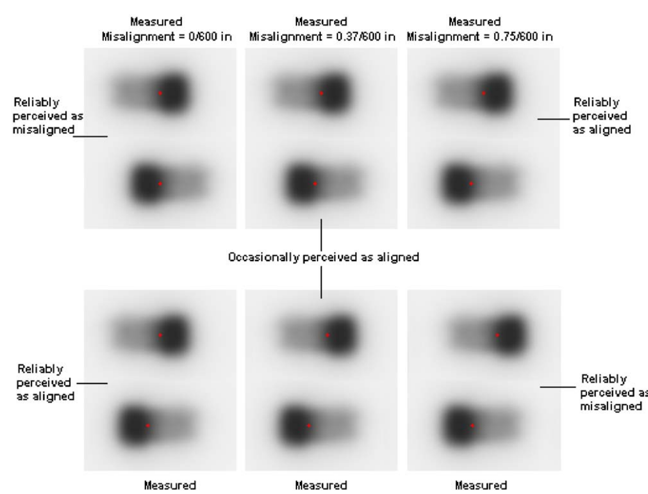

Figure 29. Measured alignment versus perceived alignment for 45 ips bidirectional print mode. Measured misalignment increases from left to right and from top to bottom. The white cross indicates the location of the centroid in each average dot profile.

tance corresponds to a straight vertical line in the scanned interswath junctures, which has also been highlighted with the middle (green) dotted line in Fig. 27. This suggests that the main cue to perceived alignment is the position at which the edges of the lines reach a certain locally averaged level of absorptance and, more specifically, the absorptance level 0.65 highlighted by the green dotted line. Notice that this absorptance level corresponds roughly to the 60% threshold of the transition from the paper to the line peak absorptance levels. This threshold has been reported to be the one that defines the line width perceived by the human observer.[34] For reference, two other levels of absorptance have been highlighted as well.

Figure 29 shows a simulation of dot-level relationships between swaths, specifically, at the interswath juncture. The average dot profile for a single direction at a print speed of 45 ips was calculated. To account for the opposite directionality of the pen at the interswath junctures, the profile was flipped horizontally and the flipped version was placed right below the original profile. The two profiles are displaced with respect to one another to illustrate the effect of dot elongation on the relation between perceived and measured alignment. The amount of the relative displacement increases from left to right and from top to bottom in steps that correspond to the response that they elicited: from misalignment values that were consistently perceived as misaligned, to values that were occasionally perceived as misaligned, to values that were consistently perceived as aligned.

The first image in the sequence shows the relationship between two dots with perfectly aligned horizontal centroids in a configuration that was consistently perceived as misaligned. The next image in the sequence shows the situation where the horizontal centroids are displaced 0.37/600 in. with respect to one another in a configuration that was occasionally perceived as aligned. The last image in the top row illustrates the situation where the horizontal displacement between the dot centroids equals 0.75/600 in. This is the offset that was consistently perceived as aligned by the subjects for this particular print mode. The bottom row illustrates displacements that continue to increase, starting from the offset that was reliably perceived as aligned and ending with an offset that was again reliably perceived as misaligned. Figure 30 shows a similar sequence in coarser steps for the 60 ips print mode. These sequences of images are an alternative way of visualizing the fact that the main cue to perception of alignment is not the offset between centroids, since zero offset between dot centroids does not guarantee that the dot configuration will be perceived as aligned. Rather, subjects appear to base their decision on the overall dot shape including tails or satellites.

Sensitivity to Changes in Alignment

The constant stimuli test results allowed us to estimate two important parameters of alignment detection: the point of perceived perfect alignment and the sensitivity to detect differences in alignment. The estimation of the sensitivity via constant stimuli tests is not reliable for the reasons explained earlier. This raised the need for signal detection tests that provide a means to reliably measure sensitivity. The results showed that subjects are less sensitive to changes in alignment with the 60 ips print mode than with any other mode.

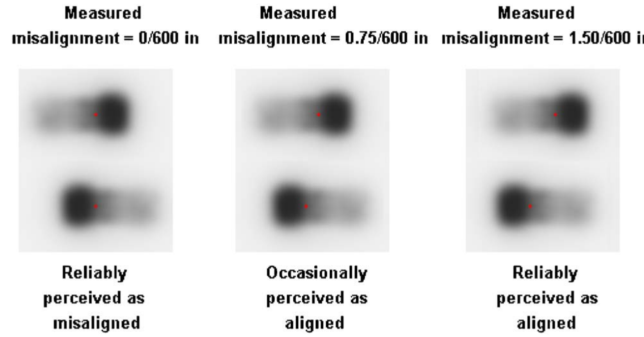

Figure 30. Measured alignment versus perceived alignment for 60 ips bidirectional print mode. Measured misalignment increases from left to right. The white cross indicates the location of the centroid in each average dot profile.

CONCLUSIONS

We presented a combination of automated image analysis methods and psychophysical tests to shed light on the issue of how swath-to-swath ink jet alignment is perceived by the average observer. We developed algorithms to measure misalignment as printed on a page and to classify printed dots based on their characteristics. Using the tools we developed, we showed that dot variability from pen to pen is negligible. We demonstrated that the way alignment is perceived is highly dependent on the characteristics of the individual dots. As print speed increases, dot elongation increases and the presence of artifacts like tails and satellites becomes more evident. At small print speeds, dot shape tends to be symmetric about its centroid, and alignment of dot centroids corresponds roughly to alignment of dot outlines. At higher print speeds, dot shape becomes asymmetric about the dot centroid. In these cases, perfect alignment is not achieved by aligning dot centroids, but rather by aligning outlines at a certain level of absorptance. For the printer manufacturer, this implies that there is a need to develop alignment techniques that are based on alignment of ink outlines rather than on alignment of absorptance centroids. This conclusion corresponds to the results reported by Ward et al.,[35] where the authors concluded that the subjects primarily used virtual edges to judge misalignment between two random dot clusters.

Recall that the just noticeable angular offset between two line segments is called Vernier acuity and that it ranges from 5 to 10 seconds of arc. The sensitivity thresholds for perception of changes in alignment reported in this paper are within the order of the Vernier acuity: 0.2/600 in., the estimated DL for the 15, 30 and 45 ips print mode with the signal detection test, corresponds to 5.7 seconds of arc at a viewing distance of 12 in. On the other hand, 0.4/600 in., the estimated DL for the 60 ips print mode with the signal detection test, corresponds to 11.5 seconds of arc at a viewing distance of 12 in. It is important to emphasize, however, that these thresholds do not remain unchanged as printing speed changes. Specifically, the sensitivity threshold is noticeably higher when carriage speeds go beyond 45 ips. This result was corroborated by the results of the psychophysical tests and corresponds to results reported by Patel et al.,[18] where the authors found that Vernier thresholds increase for dots with irregular shapes.

ACKNOWLEDGMENTS

The authors wish to thank Stuart Scofield, Bret Taylor, and Steve Walker of HP Vancouver, WA for their invaluable assistance and encouragement during the performance of this research. This work was supported by the Hewlett-Packard Company.

REFERENCES

1 "Document B 123: NP 13660. Measurement of image quality attributes for hardcopy output", 7th Working Draft, ISO/IEC, Geneva, Switzerland, 1995.
2 Y. Kipman, "Image quality metrics for printers/plotters", *Proc. IS&T/SID's Fourth Color Imaging Conference* (IS&T, Springfield, VA, 1995) pp. 134–138.
3 Y. Kipman, "Image quality metrics for printers and media", in *Proc. IS&T's PICS: Image Processing, Image Quality, Image Capture, Systems Conference* (IS&T, Springfield, VA, 1998) pp. 183–187.
4 D. Wolin, K. Johnson, and Y. Kipman, "The importance of objective analysis in image quality evaluation", *Proc. IS&T's NIP 14* (IS&T, Springfield, VA, 1998) pp. 603–606.
5 D. Aultman and R. Dumas, "Automating jet quality analysis using a scanner-based system", *Proc. IS&T's NIP 20* (IS&T, Springfield, VA, 2004) pp. 378–382.
6 D. Forrest, J. Briggs, and M. Tse, "Print quality analysis as a QC tool for manufacturing inkjet print heads", *Proc. IS&T's NIP 14* (IS&T, Springfield, VA, 1998) pp. 590–594.
7 D. Wolin, K. Johnson, and Y. Kipman, "Automating image quality analysis", *Proc. IS&T's NIP 14* (IS&T, Springfield, VA, 1998) pp. 627–630.
8 J. Briggs, M. Murphy, and Y. Pan, "Banding characterization for inkjet printing", *Proc. IS&T's PICS: Image Processing, Image Quality, Image Capture, Systems Conference* (IS&T, Springfield, VA, 2000) pp. 84–88.
9 Y. Kipman and K. Johnson, "Dot placement analysis using a line scan camera and rigid body rotation", *Proc. IS&T's PICS: Image Processing, Image Quality, Image Capture, Systems Conference* (IS&T, Springfield, VA, 2001) pp. 68–71.
10 P. Fleming, J. Cawthorne, F. Mehta, S. Halwawala, and M. K. Joyce, "Interpretation of dot area and dot shape of inkjet dots based on image analysis", J. Imaging Sci. Technol. **47**, 394–399 (2003).
11 S. Wang, "Aerodynamic effect on inkjet main drop and satellite dot placement", *Proc. IS&T's NIP 14* (IS&T, Springfield, VA, 1998) pp. 5–8.
12 J. P. Allebach, "DBS: Retrospective and future directions", Proc. SPIE **4300**, 358–376 (2001).
13 D. Kacker, T. Camis, and J. Allebach, "Electrophotographic process embedded in direct binary search", IEEE Trans. Image Process. **11**, 243–257 (2002).
14 F. Baqai and J. Allebach, "Halftoning via direct binary search using analytical and stochastic printer models", IEEE Trans. Image Process. **12**, 1–15 (2003).
15 J. Lee and J. P. Allebach, "Inkjet printer model based halftoning", IEEE Trans. Image Process. **4**, 674–689 (2005).
16 J. Yen, M. Carlsson, M. Chang, J. Garcia, and H. Nguyen, "Constraint solving for inkjet print mask design", J. Imaging Sci. Technol. **44**, 391–397 (2000).
17 D. Regan, *Human Perception of Objects*, 1st ed. (Sinauer, Toronto, 2000) pp. 45–49.
18 S. Patel, H. Bedell, and M. Ukwade, "Vernier judgments in the absence of regular shape information", Vision Res. **39**, 2349–2360 (1999).
19 W. Jang and J. P. Allebach, "Characterization of printer MTF", J. Imaging Sci. Technol. **50**, 264–275 (2006).
20 J. Grice and J. P. Allebach, "The print quality toolkit", J. Imaging Sci. Technol. **43**, 187–199 (1999).
21 N. Otsu, "A threshold selection method from gray-level histograms", IEEE Trans. Syst. Man Cybern. **9**, 62–66 (1979).
22 A. Bjork, *Numerical Methods for Least Squares Problems* (Society for Industrial and Applied Math, Philadelphia, 1996).
23 K. Fukunaga, *Introduction to Statistical Pattern Recognition*, 2nd ed. (Academic, Boston, 1990).
24 M. Turk and A. Pentland, "Eigenfaces for face recognition", J. Cogn Neurosci. **3**, 71–86 (1991).
25 V. Caselles, F. Catte, T. Coll, and F. Dibos, "A geometric model for active contours", Numer. Math. **66**, 1–31 (1993).
26 M. Kass, A. Witkin, and D. Terzopoulos, "Snakes: Active contour models", Int. J. Comput. Vis. **1**(4), 321–331 (1987).
27 V. Leavers, *Shape Detection in Computer Vision Using the Hough Transform*, 1st ed. (Springer, New York, 1992).
28 H. Yuen, J. Illingworth, and J. Kittler, "Detecting partially occluded ellipses using the Hough transform", Image Vis. Comput. **7**, 31–37 (1989).
29 A. Fitzgibbon, M. Pilu, and R. Fisher, "Direct least square fitting of ellipses", IEEE Trans. Pattern Anal. Mach. Intell. **21**, 476–480 (1999).
30 R. Halif and J. Flusser, "Numerically stable direct least squares fitting of ellipses", *Proc. Sixth Int'l Conf. Computer Graphics and Visualization*, Vol. 1, 125–132 (1998).
31 G. Gescheider, *Psychophysics: Method, Theory, and Application*, 2nd ed. (Erlbaum, Hillsdale, NJ, 1985).
32 D. Finney, *Probit Analysis*, 3rd ed. (Cambridge University Press, New York, 1971).
33 N. Macmillan and C. Creelman, Eds., *Detection Theory: A User's Guide*, 2nd ed. (LEA, New York, 2005) pp. 3–50.
34 P. Engeldrum, "Quality of dot formed images", Proc. SPIE **310**, 118–124 (1981).
35 R. Ward, C. Casco, and R. Watt, "The location of noisy visual stimuli", Can. J. Psychol. **39**, 387–399 (1985).